Monthly Notices of the ROYAL ASTRONOMICAL SOCIETY
MNRAS **512,** 2508–2524 (2022) https://doi.org/10.1093/mnras/stac615

Wide-band view of high-frequency quasi-periodic oscillations of GRS 1915+105 in 'softer' variability classes observed with *AstroSat*

Seshadri Majumder,[1]★ H. Sreehari,[2] Nafisa Aftab,[1] Tilak Katoch,[3] Santabrata Das[1]★ and Anuj Nandi[4]★

[1]*Department of Physics, Indian Institute of Technology Guwahati, Guwahati, 781039, India*
[2]*Indian Institute of Astrophysics, Bangalore, 560034, India*
[3]*Department of Astronomy and Astrophysics, Tata Institute of Fundamental Research, Colaba, Mumbai, 400005, India*
[4]*Space Astronomy Group, ISITE Campus, U R Rao Satellite Centre, Outer Ring Road, Marathahalli, Bangalore, 560037, India*

Accepted 2022 March 3. Received 2022 March 3; in original form 2021 September 27

ABSTRACT

We present a comprehensive temporal and spectral analysis of the 'softer' variability classes (i.e. θ, β, δ, ρ, κ, ω and γ) of the source GRS 1915+105 observed by *AstroSat* during the 2016−2021 campaign. Wide-band (3−60 keV) timing studies reveal the detection of high-frequency quasi-periodic oscillations (HFQPOs) with frequencies of 68.14−72.32 Hz, significance of 2.75−11σ and rms amplitude of 1.48–2.66 per cent in δ, κ, ω and γ variability classes. Energy-dependent power spectra show that HFQPOs are detected only in the 6−25 keV energy band and rms amplitude is found to increase (1–8 per cent) with energy. The dynamical power spectra of the κ and ω classes demonstrate that HFQPOs seem to be correlated with high count rates. We observe that wide-band (0.7−50 keV) energy spectra can be described by the thermal Comptonization component (`nthComp`) with a photon index ($\Gamma_{\rm nth}$) of 1.83−2.89 along with an additional steep ($\Gamma_{\rm PL} \sim 3$) power-law component. The electron temperature ($kT_{\rm e}$) of 1.82−3.66 keV and optical depth (τ) of 2−14 indicate the presence of a cool and optically thick corona. In addition, `nthComp` components, $1.97 \lesssim \Gamma_{\rm nth} \lesssim 2.44$ and $1.06 \times 10^{-8} \lesssim F_{\rm nth}$ (erg cm^{-2} s^{-1}) $\lesssim 4.46 \times 10^{-8}$, are found to dominate in the presence of HFQPOs. Overall, these findings infer that HFQPOs are possibly the result of the modulation of the 'Comptonizing corona'. Further, we find that the bolometric luminosity (0.3−100 keV) of the source lies within the sub-Eddington (3–34 per cent $L_{\rm Edd}$) regime. Finally, we discuss and compare the obtained results in the context of existing models on HFQPOs.

Key words: accretion, accretion discs – black hole physics – stars: individual: GRS 1915+105 – X-rays: binaries.

1 INTRODUCTION

Black hole X-ray binaries (BH-XRBs) occasionally exhibit high-frequency quasi-periodic oscillation (HFQPO) features that are potentially viable to probe the effect of strong gravity in the vicinity of compact objects. The signature of QPOs is observed as a narrow feature with excess power in the power density spectrum (van der Klis 1988). In general, QPO frequencies are classified in two different categories in BH-XRB systems: (i) low-frequency QPOs (LFQPOs) with centroid frequency $\nu_{\rm QPO} < 40$ Hz; (ii) high-frequency QPOs (HFQPOs) with $\nu_{\rm QPO}$ exceeding 40 Hz (Remillard & McClintock 2006). LFQPOs are common in BH-XRB systems, whereas HFQPOs are detected in few BH-XRBs observed with *RXTE*,[1] such as GRS 1915+105 (65−69 Hz; Morgan, Remillard & Greiner 1997; Belloni & Altamirano 2013a), GRO J1655−40 (300 and 450 Hz; Remillard et al. 1999, 2002; Strohmayer 2001a), XTE J1550−564 (102−284 Hz, Homan et al. 2001; 188 and 249−276 Hz, Miller et al. 2001), H 1743−322 (160 and 240 Hz, Homan et al. 2005; 166, 239 and 242 Hz, Remillard et al. 2006), XTE J1650−500 (50 and 250 Hz; Homan et al. 2003), 4U 1630−47 (100−300 Hz; Klein-Wolt, Homan & van der Klis 2004), XTE J1859+226 (150 and 187 Hz; Cui 2000) and IGR J17091−3624 (66 and 164 Hz; Altamirano & Belloni 2012). However, the detection of HFQPOs in XTE J1650−500, 4U 1630−47 and XTE J1859+226 remains inconclusive because of their broad features with lesser significance (Belloni, Sanna & Méndez 2012).

The HFQPOs are detected by *RXTE* in high flux observations with intermediate hardness ratios. However, it is intriguing that not all observations with high flux show this feature (Belloni et al. 2012). Typically, HFQPOs are observed with either one or two peaks in power spectra and the corresponding centroid frequencies are found to vary with time (Belloni & Stella 2014). In some instances, the simultaneous observations of HFQPOs of ∼3 : 2 frequency ratio are reported in GRO J1655−40 and H1743−322 (Strohmayer 2001a; Remillard et al. 2002), which are possibly yielded due to the resonance between two epicyclic oscillation modes (Abramowicz & Kluźniak 2001). Further, the fractional variabilities (i.e. rms amplitudes) of HFQPOs, detected in various sources, are found to increase with energy (Miller et al. 2001). In particular, for GRS 1915+105, the percentage rms (hereafter rms%) associated with 67 Hz increases from 1.5 per cent (at ∼5 keV) to 6 per cent (at ∼20 keV; Morgan et al. 1997). In addition, Homan et al. (2001) measured time lags for ∼282-Hz HFQPOs and found either zero or negative time lags (soft

★ E-mail: smajumder@iitg.ac.in (SM); sbdas@iitg.ac.in (SD); anuj@ursc.gov.in (AN)
[1]https://heasarc.gsfc.nasa.gov/docs/xte/XTE.html

photons lag hard photons) for the XTE J1550−564 source. Also, hard phase lags (hard photons lag soft photons) were observed for 67-Hz HFQPOs in GRS 1915+105 including other BH-XRBs as well (Cui 1999; Méndez et al. 2013). However, a negative phase lag was observed for the 35-Hz feature, which appeared simultaneously with 67-Hz HFQPOs in GRS 1915+105. Interestingly, the magnitude of these soft and hard lags are found to increase with energy (Méndez et al. 2013).

Nevertheless, the thermal and non-thermal spectral components of BH-XRB spectra reveal the characteristics of the underlying emission processes and the geometry of the accretion disc. In general, the thermal emissions mostly originate from the different radii of the multitemperature accretion disc (Shakura & Sunyaev 1973), whereas the high-energy non-thermal emissions are emanated due to inverse-Compton scattering of seed blackbody photons reprocessed at the 'hot' corona surrounding the inner part of the accretion disc (see Sunyaev & Titarchuk 1980; Chakrabarti & Titarchuk 1995; Tanaka & Lewin 1995; Mandal & Chakrabarti 2005; Iyer, Nandi & Mandal 2015; and references therein). Alternative prescriptions of the jet-based corona model are also widely discussed in the literature (Beloborodov 1999; Fender et al. 1999; Lucchini et al. 2021; Wang et al. 2021) including different coronal geometries (Haardt et al. 1993; Markoff, Nowak & Wilms 2005; Nowak et al. 2011; Poutanen, Veledina & Zdziarski 2018). Often, the presence of HFQPOs is found to be prominent largely in the softer states dominated by the disc emission (McClintock & Remillard 2006). Therefore, it is important to carry out the wide-band spectral modelling in the presence of HFQPO features.

GRS 1915+105, known as a microquasar (Mirabel & Rodríguez 1994), is a very bright BH-XRB system that was discovered in 1992 by the *GRANAT* mission (Castro-Tirado, Brandt & Lund 1992). The source possibly harbours a fast-spinning Kerr black hole (McClintock & Remillard 2006) with spin >0.98 measured by indirect means (see Sreehari et al. 2020 and references therein). The mass and distance of the black hole are constrained as $12.4^{+2.0}_{-1.8}$ $M_{\odot}$ and 8.6 kpc, respectively (Reid et al. 2014). Interestingly, GRS 1915+105 shows different types of structured variabilities in its light curves with a time-scale of seconds to minutes, and these are identified and put into 14 distinct classes (Belloni et al. 2000, Klein-Wolt et al. 2002, Hannikainen et al. 2005). Meanwhile, *RXTE* extensively observed both LFQPOs (see Nandi et al. 2001; Vadawale, Rao & Chakrabarti 2001; Ratti, Belloni & Motta 2012; and references therein) and HFQPOs (Morgan et al. 1997; Strohmayer 2001a; Belloni et al. 2006; Belloni & Altamirano 2013a; Méndez et al. 2013) in this source. Morgan et al. (1997) first detected HFQPOs with frequencies of 65−67 Hz in GRS 1915+105 observed with *RXTE*. Belloni et al. (2006) reported the detection of HFQPOs with a frequency 170 Hz in the θ class, whereas HFQPOs with frequencies of 63−71 Hz are also observed in the κ, γ, μ, δ, ω, ρ and ν classes (Belloni & Altamirano 2013a). Simultaneous detections of 34- and 41-Hz features with the fundamental HFQPO at ∼68 Hz were also reported with *RXTE* (Strohmayer 2001b; Belloni & Altamirano 2013b).

Recently, using *AstroSat* observations, Belloni et al. (2019) and Sreehari et al. (2020) observed HFQPOs with frequencies of 67.4−72.3 and 67.96−70.62 Hz in GRS 1915+105, respectively. Belloni et al. (2019) studied the temporal properties of GRS 1915+105 considering only two variability classes from 2017 observations. They found a direct correlation between the centroid frequency of HFQPOs and hardness, including positive phase lags that were found to increase with energy and decrease with hardness. However, they did not investigate the spectral characteristics of the source. Further, Sreehari et al. (2020) observed the gradual decrease of the strength of the HFQPO features in the δ class, which eventually disappear with the increase of the count rate and the decrease of the hardness ratio. They also infer that HFQPOs are present in the 6−25 keV energy range and ascertain that the HFQPOs in GRS 1915+105 seem to be yielded due to an oscillating Comptonized 'compact' corona surrounding the central source.

In this paper, for the first time to the best of our knowledge, we carry out in-depth analysis and modelling of wide-band *AstroSat* observations of eight variability classes (θ, β, δ, ρ, κ, ω, γ and χ) of GRS 1915+105 during 2016−2021 to study the HFQPO features. While doing so, we examine the colour–colour diagram by defining the soft colour (HR1, ratio of count rates in 6−15 keV to 3−6 keV) and hard colour (HR2, ratio of count rates in 15−60 keV to 3−6 keV). Adopting the selection criteria for the 'softer' variability classes as $0.02 \lesssim \mathrm{HR2} \lesssim 0.11$ and $0.61 \lesssim \mathrm{HR1} \lesssim 0.90$, and 'harder' variability class with $\mathrm{HR2} > 0.11$ and $\mathrm{HR1} \gtrsim 0.7$, we find seven 'softer' variability classes, namely δ, ρ, κ, ω, γ, β and θ, respectively. Subsequently, we examine the light curves and study the energy-dependent HFQPO features, rms% variabilities, and dynamic power spectra using Large Area X-ray Proportional Counter (LAXPC) observations. We find HFQPO features in the δ, κ, ω and γ variability classes, whereas no such HFQPO signatures are seen in the θ, β, ρ and χ classes. We model the wide-band (0.7−50 keV) energy spectra by combining the Soft X-ray Telescope (SXT) and LAXPC data to understand the characteristics of the emission processes. Finally, we attempt to correlate the temporal and spectral parameters to explain the underlying mechanism responsible for the generation of the HFQPO phenomenon in the 'softer' variability classes of GRS 1915+105 observed with *AstroSat*.

The paper is organized as follows. In Section 2, we discuss the observations and data reduction procedures of the SXT and LAXPC instruments. In Section 3, we present the characteristics of different variability classes (i.e. θ, β, δ, ρ, κ, ω, γ and χ) and discuss the results of both static and dynamic analyses of the power density spectra. Results from wide-band spectral analysis with and without HFQPO features are presented in Section 4. We discuss the results from spectro-temporal correlation in Section 5. In Section 6, we present a discussion based on the results from temporal and spectral studies in the context of the existing models of HFQPOs for BH-XRBs. Finally, we conclude in Section 7.

2 OBSERVATION AND DATA REDUCTION

India's first multiwavelength space-based observatory *AstroSat* (Agrawal 2006) provides a unique opportunity to observe various astrophysical objects in the X-ray band of the 0.3−100 keV energy range. It consists of three basic X-ray instruments: the SXT (Singh et al. 2017), the LAXPC (Yadav et al. 2016; Agrawal et al. 2017; Antia et al. 2017) and the Cadmium Zinc Telluride Imager (CZTI; Vadawale et al. 2016). The source GRS 1915+105 was observed by *AstroSat* for 47 pointed observations (termed ObsIDs) during different time periods during 2016−2021. In this work, we examine all 47 ObsIDs that include 38 Guaranteed Time (GT) data, four Announcement of Opportunity (AO) cycle data and five Target of Opportunity (TOO) cycle data of the LAXPC and SXT instruments. These observations exhibit all together seven 'softer' (θ, β, δ, ρ, κ, ω and γ) and one 'harder' (χ) variability classes, respectively. In order to avoid repetition of results from identical variability classes, we consider 24 orbits from 17 ObsIDs, as delineated in Table 1.

Table 1. Observation details of the source GRS 1915+105 observed by *AstroSat* during 2016– 2021 in seven 'softer' and one 'harder' variability classes. In the table, ObsID along with MJD, orbit number and exposure time are given. The detected ($r_{\rm det}$) and incident ($r_{\rm in}$) count rates of the LAXPC detector along with hardness ratios are also tabulated. In the HR1 and HR2 columns, A, B and C are the count rates in the 3−6, 6−15 and 15−60 keV energy ranges, respectively (see Sreehari et al. 2020). MJD 57451 corresponds to 2016 March 4. See text for details.

ObsID	MJD	Orbit	Effective exposure (s)	$r_{\rm det}$ (cts s^{-1})	$r_{\rm in}$ (cts s^{-1})	HR1 (B/A)	HR2 (C/A)	Variability class	HFQPO
T01_030T01_9000000358	57451.89	2351	3459	7252	8573	0.68	0.07	θ	No
	57452.82	2365	3148	4376	4825	0.69	0.09	χ	No
	57453.35	2373	1099	8915	10997	0.69	0.09	θ	No
G05_214T01_9000000428	57504.02	3124	2533	7308	8651	0.76	0.04	ω	Yes
G05_189T01_9000000492	57552.56	3841	3027	7965	9588	0.75	0.03	δ	No
	57553.88	3860	2381	6744	7872	0.87	0.06	δ	Yes
G06_033T01_9000000760	57689.10	5862	2674	5359	6047	0.62	0.04	β	No
G06_033T01_9000000792	57705.22	6102	3633	6712	7829	0.68	0.02	δ	No
G07_028T01_9000001232	57891.88	8863	3228	1431	1476	0.73	0.11	ρ'	No
G07_046T01_9000001236	57892.74	8876	3627	1292	1328	0.61	0.09	ρ	No
G07_028T01_9000001370	57943.69	9629	977	2814	2993	0.76	0.04	κ	No
	57943.69	9633	3442	2701	2866	0.75	0.04	κ	Yes
G07_046T01_9000001374	57946.10	9666	1093	3115	3335	0.79	0.04	κ	Yes
	57946.34	9670	2735	3160	3387	0.79	0.04	κ	Yes
G07_028T01_9000001406	57961.39	9891	1323	3642	3947	0.86	0.07	κ	No
	57961.39	9894	2451	4415	4872	0.87	0.05	κ	Yes
G07_046T01_9000001408	57961.59	9895	3590	4726	5254	0.87	0.05	κ	Yes
G07_028T01_9000001500	57995.30	10394	3036	5719	6511	0.90	0.06	ω	Yes
G07_046T01_9000001506	57996.46	10411	3632	6160	7088	0.88	0.05	ω	Yes
G07_046T01_9000001534	58007.80	10579	1729	6968	8180	0.84	0.05	ω	Yes
	58008.08	10583	1898	7392	8769	0.88	0.05	γ	Yes
A04_180T01_9000001622	58046.36	11154	2059	7312	8657	0.66	0.02	δ	No
A04_180T01_9000002000	58209.13	13559	2632	1403	1445	0.87	0.19	χ	No
A05_173T01_9000002812	58565.82	18839	3626	300	302	1.02	0.28	χ	No

2.1 Soft X-ray Telescope

The SXT is a charged coupled device (CCD) based X-ray imaging instrument onboard *AstroSat* in the energy range of 0.3−8 keV, which operates both in fast window (FW) and photon counting (PC) modes. SXT data are analysed following the guidelines provided by the SXT instrument team.[2] We obtain level-2 SXT data from the Indian Space Science Data Center (ISSDC)[3] archive. For all the observations under consideration, SXT data are available in PC mode except for two observations (Orbit 3841 and 3860), which are available in FW mode. The source images, light curves and spectra are generated from level-2 cleaned event file using XSELECT v2.4g in HEASOFT v6.26.1. While examining the pile-up effect, we find that the source counts are less than 0.5 cts pixel^{-1} frame^{-1} and less than 40 cts s^{-1} in the central 1-arcmin circular region of the image. Hence, we do not incorporate the pile-up correction in our analysis, following the *AstroSat Handbook*[4] (for details, see also Baby et al. 2020; Katoch et al. 2021). Further, we consider two scenarios of 12-arcmin and 14-arcmin circular regions concentric with the source coordinate for PC mode data. Extracting source counts within these two regions separately, we find that the 12-arcmin region contains up to 90 per cent of the total photon counts. Hence, in our analysis, we choose the 12-arcmin circular region as the source region (Fig. 1) for all the PC mode data and we extract the source images, light curves and spectra from this region. For the observations corresponding to FW mode data, we find that the source was offset in the CCD frame (Sreehari et al. 2020). Because of this, we choose the source region as the 5-arcmin circular region for these two observations. As the timing resolution (∼2.38 s) of the SXT is poor compared with the LAXPC, we use SXT data only for the spectral analysis. In this work, we use the SXT instrument response file, the background spectrum file and the ancillary response file (ARF) for both PC and FW mode data provided by the SXT instrument team.[5]

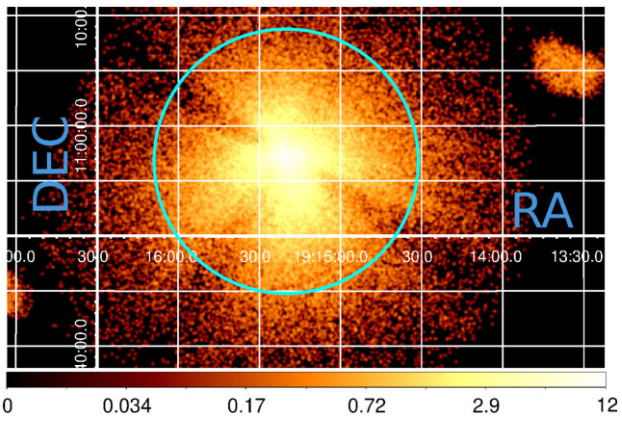

Figure 1. SXT image of the source GRS 1915+105 obtained with the PC mode data in ω class observation on MJD 57995.30 (Orbit 10394). The cyan circle corresponds to the 12-arcmin circular region, which is considered as the source region. The colour denotes the intensity distribution of the source. See text for details.

[2] https://www.tifr.res.in/~astrosat_sxt/index.html
[3] https://webapps.issdc.gov.in/astro_archive/archive/Home.jsp.
[4] http://www.iucaa.in/~astrosat/AstroSat_handbook.pdf.
[5] https://www.tifr.res.in/~astrosat_sxt/dataanalysis.html.

2.2 Large Area X-ray Proportional Counter

The LAXPC is a proportional counter consisting of three identical detectors, LAXPC10, LAXPC20 and LAXPC30, which have a combined effective area of 6000 cm^2. It operates in the 3−80 keV energy range (Yadav et al. 2016; Agrawal et al. 2017; Antia et al. 2017). All three LAXPC detectors have a temporal resolution of 10 μs, which offers rich timing analysis compared with the SXT. We use LAXPC level-1 data in the event analysis mode available in the *AstroSat* public archive[3] for timing as well as spectral analyses. The details of the LAXPC data extraction procedure and analysis methods are given in Sreehari et al. (2019, 2020). The software LAXPCSOFT v3.4[6] (Antia et al. 2017), released on 2021 June 14, is used to process the level-1 data to level-2 data. We extract data from the top layer of the detector and consider only single events in our analysis. Further, we choose the background models, which are generated closest to the observation dates. While performing data extraction, the LAXPC instrument response files are generated following Antia et al. (2017). The software generates the Good Time Interval (GTI) of the data consisting of the observation's time information excluding the data gap due to Earth's occultation and the South Atlantic Anomaly (SAA). The longest continuous observation in each orbit is considered in the present analysis (see Table 1). Background-subtracted LAXPC10 and LAXPC20 combined light curves of 1-s time resolution in different energy ranges are generated by choosing the corresponding LAXPC channels using the standard routine of the software. It should be noted that we extract the source spectra from LAXPC20 data only because the gain remains stable throughout the entire observational period (Antia et al. 2021).

3 TIMING ANALYSIS AND RESULTS

3.1 Variability classes and colour–colour diagram

We generate 1-s binned light curves in the energy range 3−60 keV, after combining the data from LAXPC10 and LAXPC20 while studying the structured variability in different classes. Following Agrawal et al. (2018) and Sreehari et al. (2019, 2020), we correct the dead-time effect in all the light curves and calculate the average incident and detected count rates in the 3−60 keV energy range, as tabulated in Table 1. The light curves are generated in the 3−6, 6−15 and 15−60 keV energy ranges to plot the CCDs. We define the soft colour and hard colour following Sreehari et al. (2020) as HR1 = B/A and HR2 = C/A, where A, B and C are the photon count rates in the 3−6, 6−15 and 15−60 keV energy bands, respectively. The CCDs are obtained by plotting HR1 against HR2. It should be noted that the combined LAXPC10 and LAXPC20 background count rate (∼225 cts s^{-1}) is negligible (∼2.5 per cent) compared to the combined source count rate (∼10 000 cts s^{-1}). Accordingly, we incorporate the background correction while carrying out the colour–colour and spectral analyses. However, power spectra are generated without background correction of light curves.

Following the classification scheme of Belloni et al. (2000), the light curves and CCDs indicate the presence of seven 'softer' variability classes $\theta, \beta, \delta, \rho, \kappa, \omega$ and γ with an additional variant (ρ') of the ρ class (Athulya et al. 2022), and one 'harder' variability class (χ). The hardness ratios HR1 and HR2 for each class are tabulated in Table 1. It is clearly seen that the soft colour HR1 and the hard colour HR2 are generally less than 0.9 and 0.1, respectively, which imply the 'softer' variability classes. In Fig. 2, we present background-subtracted and dead-time corrected LAXPC light curves of eight different variability classes (θ, β, δ, ρ, κ, ω, γ and χ) with the CCD at the top-left inset of each panel. Different structured variability patterns along with the variations in the CCDs are observed in various classes.

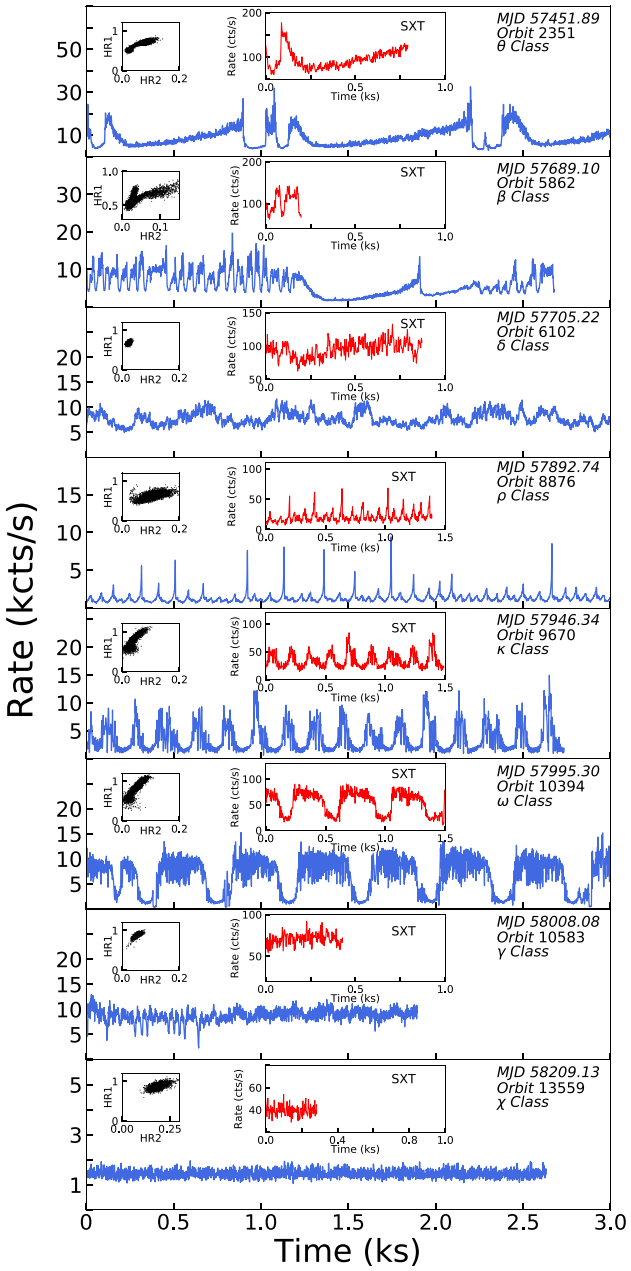

Figure 2. Background-subtracted and dead-time corrected 1-s binned light curves of GRS 1915+105 observed with *AstroSat*. In the panels, light curves corresponding to eight different variability classes (i.e. θ, β, δ, ρ, κ, ω, γ and χ) are depicted from top to bottom. Each light curve is obtained by combining LAXPC10 and LAXPC20 data in the 3−60 keV energy band. In every panel, the CCD and the SXT light curves (0.5−7 keV) are also shown in the top-left and top-middle insets, respectively. See text for details.

During the *AstroSat* campaign, the source was initially observed in the θ variability class (see Banerjee et al. 2021), where the count rate went up to 20 kcts s^{-1} and both colours are softened as observed in the CCD. Further, the source was found in the ω, δ and β variability classes (see Table 1.) Subsequently, the source was found in a variability class ρ on MJD 57892.74. In this period,

[6] http://www.tifr.res.in/~astrosat_laxpc/LaxpcSoft.html

we see a 'flare'-like nature in the light curve and, in the CCD, the points are distributed more towards the harder range. Next, the source displayed the κ class variability, in which the count rates were high as 15 kcts s^{-1} and multiple 'dips' (low counts) of a few tens to a hundred seconds of duration are observed. In addition, small duration ($\sim$ a few seconds) 'non-dips' (high counts) are also present between the two 'dips'. The CCD shows a uniform C-shaped distribution of points. In the ω class, the duration of 'non-dips' between the two 'dips' increases up to a few hundred seconds, and the CCD shows a similar pattern as observed in the κ class. In the γ class, the long-duration 'dips' are absent; instead, small 'dips' with a duration of a few seconds are observed along with high counts. A diagonally elongated distribution of points is found in the CCD. Finally, the source was found in the 'harder' variability class (χ) with a count rate less than 1.5 kcts s^{-1} (Athulya et al. 2022). In each panel of Fig. 2, we show the SXT light curves of the same observations in the energy range of 0.5−7 keV in the top-middle inset. Similar structured variabilities are also observed in the SXT light curves as seen in the LAXPC observations.

3.2 Static power density spectra

We generate light curves of 1-ms resolution corresponding to each variability class with combined data from LAXPC10 and LAXPC20. We generate a power density spectrum (PDS) for each observation considering a Nyquist frequency of 500 Hz with these light curves. We choose 32 768 bins per interval for generating the respective PDS, which are further averaged to obtain the final PDS. A geometric binning factor of 1.03 is used for the power spectral analysis. Finally, the dead-time corrected power spectra are obtained following Agrawal et al. (2018) and Sreehari et al. (2019, 2020).

Each PDS, in units of (rms mean^{-1})^2 Hz^{-1}, is then modelled using multiple Lorentzians and a constant component in the wide frequency range of 0.01−500 Hz. Each Lorentzian is represented by three parameters: centroid (*LC*), width (*LW*) and normalization (*LN*). In Fig. 3, we present the model-fitted PDS of the δ, κ, ω and γ variability classes with the detected HFQPO feature as depicted in the inset of each panel. The variability class and the observation details are marked in each panel. First, we begin with the modelling of the power spectrum of the γ class observation using the model combination of a constant and four Lorentzians. Initially, two zero centroid Lorentzians and one Lorentzian with a centroid frequency at 2.25 Hz along with a constant component are used to fit the entire PDS. The fit results in a $\chi^2_{\rm red}$ of 310/234 = 1.32. Furthemore, to model the HFQPO feature, we include an additional Lorentzian with the centroid frequency of ∼72 Hz. We emphasize that while modelling the entire PDS and estimating the errors associated with the model parameters, all the model parameters are kept free. The best fit is obtained with a $\chi^2_{\rm red}$ of 133/231 = 0.58 (see also Sreehari et al. 2020). We follow the above procedure to fit the PDS in the presence of HFQPO features for the δ, κ and ω classes, and the best-fitting model parameters along with errors are tabulated in Table 2. In addition, we also note the presence of a broad feature in the PDS of δ and γ class observations at ∼1 Hz and 2 Hz, respectively, which is absent in the κ and ω classes.

The presence of the HFQPO feature in the power spectra is determined by means of quality factor ($Q = LC/LW \geq 3$) and significance ($\sigma = LN/err_{\rm neg} \geq 3$), where *LC*, *LW*, *LN* and $err_{\rm neg}$ denote the centroid frequency, width, normalization and negative error of normalization of the fitted Lorentzian function (see Sreehari et al. 2020, and references therein). The best-fitting PDS of the γ class observation shows a strong signature of the HFQPO feature of the centroid frequency $72.32^{+0.23}_{-0.21}$ Hz with a significance of 11σ, as

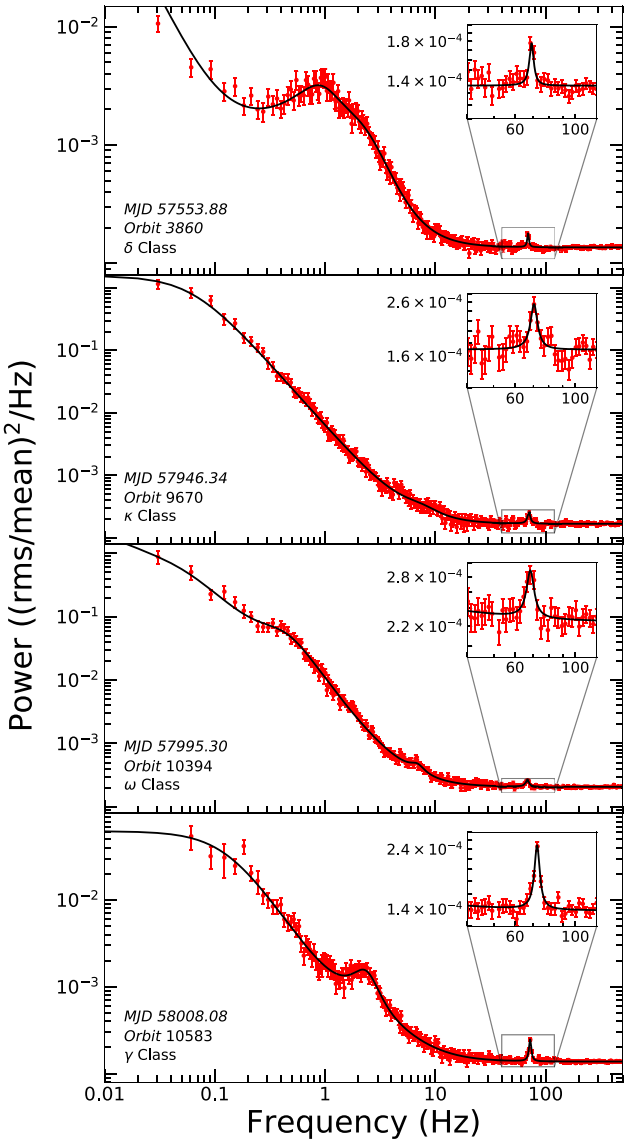

Figure 3. PDS of four different variability classes in the presence of HFQPOs. Each PDS is obtained in the 3−60 keV energy range by combining LAXPC10 and LAXPC20 observations. In each panel, variability classes are marked, and the detected HFQPO features (zoomed view) are shown in the inset. See text for details.

shown in the inset of the bottom panel of Fig. 3. We calculate the rms% of the HFQPO by taking the square root of the definite integral of the Lorentzian function (see van der Klis 1988; Ribeiro et al. 2019; Sreehari et al. 2020; and references therein) with the HFQPO fitted parameters (i.e. *LC*, *LW* and *LN*) and we obtain 2.46 ± 0.19 per cent. Further, we calculate the rms% of the entire PDS in the wide frequency range 0.01−500 Hz and for the γ class observation, we obtain its value as 12.98 ± 3.72 per cent. We detect 11 such HFQPO features in four variability classes (i.e. δ, κ, ω, γ) with centroid frequencies in the range of 68.14−72.32 Hz, significance in the range of 2.75−11.0σ and the rms% in the range of 1.48−2.66. The model-fitted as well as estimated parameters of all observations are tabulated in Table 2.

To address the non-detection of the HFQPO features, we compute the rms% amplitude of the most significant peak near the observed HFQPO frequency for all the observations. We find the highest value

Table 2. Details of the best-fitting PDS parameters from LAXPC observations of GRS 1915+105 in the 3−60 keV energy range in different variability classes. Results are obtained with combined data from LAXPC10 and LAXPC20, where CO and L_i ($i = 1, 2, 3, 4$) denote the constant and multiple Lorentzians used to obtain the best fit, σ denotes the significance of HFQPOs and $HFQPO_{rms\%}$ and $Total_{rms\%}$ represent the rms percentage of the HFQPO feature and the entire PDS. The centroid frequency (*LC*), FWHM (*LW*) and normalization (*LN*) of the detected HFQPOs are highlighted in bold font. All the errors are computed with 68 per cent confidence level. See text for details.

MJD (orbit)	Model parameters						χ^2/dof	Estimated parameters			Class
	CO (10^{-4})		L_1	L_2	L_3	L_4		σ	$HFQPO_{rms\%}$	$Total_{rms\%}$	
57451.89 (2351)[a]	$1.58^{+0.01}_{-0.01}$	*LC*	0.0	0.0	$5.05^{+0.05}_{-0.07}$	–	170/229	–	–	19.78 ± 6.78	θ
		LW	$5.47^{+0.57}_{-0.43}$	$0.90^{+0.14}_{-0.11}$	$1.09^{+0.23}_{-0.12}$	–					
		LN	$0.0034^{+0.0007}_{-0.0007}$	$0.033^{+0.004}_{-0.004}$	$0.0010^{+0.0001}_{-0.0001}$	–					
57452.82 (2365)[a]	$1.34^{+0.01}_{-0.01}$	*LC*	0.0	0.0	$3.25^{+0.02}_{-0.01}$	$6.11^{+0.08}_{-0.11}$	168/232	–	–	17.71 ± 3.59	χ
		LW	$3.94^{+0.53}_{-0.49}$	$0.85^{+0.24}_{-0.21}$	$0.44^{+0.03}_{-0.01}$	$2.36^{+0.38}_{-0.31}$					
		LN	$0.0037^{+0.0008}_{-0.0007}$	$0.0055^{+0.0007}_{-0.0008}$	$0.019^{+0.002}_{-0.001}$	$0.00077^{+0.00005}_{-0.00004}$					
57453.35 (2373)[a]	$1.53^{+0.01}_{-0.01}$	*LC*	0.0	0.0	$6.19^{+0.14}_{-0.16}$	–	137/235	–	–	20.09 ± 4.43	θ
		LW	$7.87^{+3.23}_{-1.81}$	$1.37^{+0.19}_{-0.18}$	$1.75^{+0.61}_{-0.39}$	–					
		LN	$0.0011^{+0.0009}_{-0.0006}$	$0.0303^{+0.0036}_{-0.0031}$	$0.00046^{+0.00009}_{-0.00008}$	–					
57504.02 (3124)	$1.86^{+0.01}_{-0.01}$	*LC*	0.0	$1.71^{+0.20}_{-0.21}$	$\mathbf{71.52}^{+0.36}_{-0.29}$	–	151/233	3.67	1.48 ± 0.36	21.03 ± 4.12	ω
		LW	$0.26^{+0.04}_{-0.03}$	$2.71^{+0.23}_{-0.22}$	$\mathbf{1.25}^{+0.62}_{-0.55}$	–					
		LN	$0.21^{+0.05}_{-0.04}$	$0.00097^{+0.00016}_{-0.00013}$	$\mathbf{0.00011}^{+0.00004}_{-0.00003}$	–					
57552.56 (3841)[a]	$1.39^{+0.01}_{-0.01}$	*LC*	0.0	0.0	$0.75^{+0.06}_{-0.05}$	$2.73^{+0.21}_{-0.18}$	165/231	–	–	7.64 ± 2.18	δ
		LW	$8.45^{+1.84}_{-2.25}$	$0.33^{+0.06}_{-0.05}$	$0.77^{+0.14}_{-0.11}$	$4.05^{+0.98}_{-1.24}$					
		LN	$0.00004^{+0.00001}_{-0.00001}$	$0.012^{+0.002}_{-0.001}$	$0.0014^{+0.0003}_{-0.0002}$	$0.00023^{+0.00004}_{-0.00004}$					
57553.88 (3860)	$1.36^{+0.01}_{-0.01}$	*LC*	0.0	$1.62^{+0.23}_{-0.20}$	$0.83^{+0.04}_{-0.05}$	$\mathbf{69.31}^{+0.11}_{-0.16}$	134/228	2.75	1.54 ± 0.48	9.69 ± 2.23	δ
		LW	$0.018^{+0.005}_{-0.004}$	$3.10^{+0.19}_{-0.16}$	$1.05^{+0.24}_{-0.19}$	$\mathbf{1.39}^{+0.94}_{-1.06}$					
		LN	$0.29^{+0.03}_{-0.02}$	$0.0012^{+0.0003}_{-0.0003}$	$0.0021^{+0.0003}_{-0.0003}$	$\mathbf{0.00011}^{+0.00004}_{-0.00004}$					
57689.10 (5862)[a]	$1.72^{+0.01}_{-0.01}$	*LC*	0.0	0.0	$3.59^{+0.32}_{-0.34}$	$3.35^{+0.39}_{-0.28}$	129/231	–	–	26.30 ± 6.12	β
		LW	$0.023^{+0.001}_{-0.002}$	$1.34^{+0.15}_{-0.14}$	$6.41^{+0.49}_{-0.46}$	$0.98^{+0.26}_{-0.23}$					
		LN	$5.05^{+1.45}_{-1.21}$	$0.013^{+0.002}_{-0.002}$	$0.00071^{+0.00008}_{-0.00008}$	$0.0012^{+0.0003}_{-0.0003}$					
		LC	0.0	0.0	$1.73^{+0.33}_{-0.26}$	–					

Table 2 – *continued*

MJD (orbit)			Model parameters				χ^2/dof	Estimated parameters			Class
	CO (10^{-4})		L_1	L_2	L_3	L_4		σ	HFQPO$_{rms\%}$	Total$_{rms\%}$	
57705.22 (6102)[a]	$1.37^{+0.01}_{-0.01}$	*LW*	$1.68^{+0.71}_{-0.61}$	$0.06^{+0.02}_{-0.01}$	$4.21^{+0.15}_{-0.16}$	–	154/231	–	–	11.68 ± 2.71	δ
		LN	$0.0019^{+0.0006}_{-0.0003}$	$0.16^{+0.08}_{-0.03}$	$0.00092^{+0.00021}_{-0.00023}$	–					
		LC	0.0	0.0	$5.14^{+0.04}_{-0.02}$	$10.33^{+0.18}_{-0.21}$					
57891.88 (8863)[a]	$1.48^{+0.01}_{-0.01}$	*LW*	$13.47^{+1.41}_{-1.66}$	$0.18^{+0.04}_{-0.03}$	$1.15^{+0.12}_{-0.11}$	$3.47^{+1.43}_{-0.89}$	183/232	–	–	27.38 ± 5.69	ρ'
		LN	$0.0011^{+0.0001}_{-0.0001}$	$0.42^{+0.16}_{-0.12}$	$0.0032^{+0.0003}_{-0.0002}$	$0.00042^{+0.00006}_{-0.00004}$					
		LC	0.0	0.0	$5.74^{+0.06}_{-0.05}$	$10.63^{+0.28}_{-0.23}$					
57892.74 (8876)[a]	$1.58^{+0.01}_{-0.01}$	*LW*	$3.80^{+0.81}_{-0.67}$	$0.13^{+0.05}_{-0.03}$	$1.54^{+0.15}_{-0.14}$	$8.43^{+1.18}_{-0.93}$	144/222	–	–	23.53 ± 2.70	ρ
		LN	$0.0016^{+0.0004}_{-0.0003}$	$0.71^{+0.21}_{-0.18}$	$0.0019^{+0.0002}_{-0.0001}$	$0.00043^{+0.00005}_{-0.00002}$					
		LC	0.0	–	–	–					
57943.69 (9629)[a]	$1.52^{+0.01}_{-0.01}$	*LW*	$0.14^{+0.02}_{-0.01}$	–	–	–	149/239	–	–	35.49 ± 5.35	κ
		LN	$1.26^{+0.28}_{-0.24}$	–	–	–					
		LC	0.0	0.0	$\mathbf{71.55^{+0.96}_{-0.96}}$	–					
57943.69 (9633)	$1.59^{+0.01}_{-0.01}$	*LW*	$0.13^{+0.01}_{-0.01}$	$2.21^{+0.15}_{-0.13}$	$\mathbf{5.67^{+2.76}_{-2.17}}$	–	172/234	3.71	2.14 ± 0.50	38.32 ± 6.67	κ
		LN	$1.36^{+0.24}_{-0.21}$	$0.016^{+0.002}_{-0.002}$	$\mathbf{0.000052^{+0.000019}_{-0.000014}}$	–					
		LC	0.0	$\mathbf{69.76^{+0.89}_{-0.74}}$	–	–					
57946.10 (9666)	$1.55^{+0.01}_{-0.01}$	*LW*	$0.17^{+0.02}_{-0.01}$	$\mathbf{5.01^{+2.93}_{-2.29}}$	–	–	146/237	3.27	2.55 ± 0.71	37.28 ± 6.31	κ
		LN	$1.12^{+0.26}_{-0.22}$	$\mathbf{0.000085^{+0.000042}_{-0.000026}}$	–	–					
		LC	0.0	$6.79^{+1.38}_{-1.05}$	$\mathbf{70.45^{+0.54}_{-0.53}}$	–					
57946.34 (9670)	$1.67^{+0.01}_{-0.01}$	*LW*	$0.13^{+0.01}_{-0.01}$	$7.43^{+1.69}_{-1.98}$	$\mathbf{4.67^{+1.56}_{-1.07}}$	–	142/234	5.06	2.49 ± 0.37	37.98 ± 5.35	κ
		LN	$1.55^{+0.25}_{-0.22}$	$0.000078^{+0.000021}_{-0.000014}$	$\mathbf{0.000086^{+0.000018}_{-0.000017}}$	–					
		LC	0.0	–	–	–					
57961.39 (9891)[a]	$5.46^{+0.01}_{-0.01}$	*LW*	$0.29^{+0.04}_{-0.02}$	–	–	–	147/240	–	–	31.51 ± 4.35	κ
		LN	$0.44^{+0.12}_{-0.08}$	–	–	–					
		LC	0.0	0.0	$2.14^{+0.48}_{-0.42}$	$\mathbf{71.68^{+0.84}_{-0.75}}$					
57961.39 (9894)	$1.57^{+0.01}_{-0.01}$	*LW*	$2.14^{+0.02}_{-0.01}$	$0.09^{+0.03}_{-0.02}$	$1.25^{+0.36}_{-0.31}$	$\mathbf{4.70^{+2.60}_{-2.21}}$	156/232	3.43	2.28 ± 0.63	42.31 ± 8.66	κ

Table 2 – *continued*

MJD (orbit)			Model parameters				χ^2/dof	Estimated parameters		Class
	CO (10^{-4})		L_1	L_2	L_3	L_4		σ	HFQPO$_{rms\%}$	Total$_{rms\%}$	
		LN	$0.04^{+0.01}_{-0.01}$	$1.70^{+0.84}_{-0.53}$	$0.0042^{+0.0011}_{-0.0011}$	$\mathbf{0.000072^{+0.000038}_{-0.000021}}$					
		LC	0.0	$0.72^{+0.02}_{-0.01}$	$\mathbf{70.47^{+0.69}_{-0.65}}$	–					
57961.59 (9895)	$2.11^{+0.01}_{-0.01}$	*LW*	$0.13^{+0.02}_{-0.01}$	$4.01^{+0.66}_{-0.62}$	$\mathbf{3.86^{+1.69}_{-1.32}}$	–	171/234	4.40	1.98 ± 0.41	39.38 ± 7.30	κ
		LN	$1.59^{+0.36}_{-0.28}$	$0.00105^{+0.00069}_{-0.00033}$	$\mathbf{0.000066^{+0.000017}_{-0.000015}}$	–					
		LC	0.0	$0.32^{+0.04}_{-0.02}$	$6.79^{+0.34}_{-0.24}$	$\mathbf{68.14^{+0.65}_{-0.61}}$					
57995.30 (10394)	$2.06^{+0.01}_{-0.01}$	*LW*	$0.08^{+0.02}_{-0.01}$	$0.61^{+0.03}_{-0.02}$	$2.46^{+0.91}_{-1.10}$	$\mathbf{5.42^{+1.49}_{-1.11}}$	165/231	5.55	2.25 ± 0.31	34.27 ± 9.76	ω
		LN	$1.23^{+0.59}_{-0.39}$	$0.05^{+0.01}_{-0.01}$	$0.00012^{+0.00004}_{-0.00003}$	$\mathbf{0.000061^{+0.000012}_{-0.000011}}$					
		LC	0.0	$0.11^{+0.02}_{-0.03}$	$\mathbf{70.01^{+0.56}_{-0.49}}$	–					
57996.46 (10411)	$1.75^{+0.01}_{-0.01}$	*LW*	$0.03^{+0.01}_{-0.01}$	$0.57^{+0.07}_{-0.05}$	$\mathbf{5.96^{+1.22}_{-0.99}}$	–	193/234	7.01	2.66 ± 0.29	26.45 ± 7.47	ω
		LN	$1.75^{+0.44}_{-0.23}$	$0.08^{+0.01}_{-0.01}$	$\mathbf{0.000077^{+0.000012}_{-0.000011}}$	–					
		LC	0.0	$1.89^{+0.23}_{-0.31}$	$\mathbf{72.22^{+0.49}_{-0.39}}$	–					
58007.80 (10579)	$1.83^{+0.01}_{-0.01}$	*LW*	$0.25^{+0.05}_{-0.03}$	$3.04^{+0.42}_{-0.40}$	$\mathbf{2.25^{+0.77}_{-1.48}}$	–	128/234	4.95	1.86 ± 0.37	19.01 ± 3.66	ω
		LN	$0.18^{+0.07}_{-0.03}$	$0.00068^{+0.00011}_{-0.00009}$	$\mathbf{0.000099^{+0.000032}_{-0.000020}}$	–					
		LC	0.0	0.0	$2.25^{+0.06}_{-0.05}$	$\mathbf{72.32^{+0.23}_{-0.21}}$					
58008.08 (10583)	$1.37^{+0.01}_{-0.01}$	*LW*	$9.71^{+4.19}_{-2.66}$	$0.27^{+0.03}_{-0.03}$	$1.52^{+0.23}_{-0.21}$	$\mathbf{3.61^{+0.48}_{-0.45}}$	133/231	11.00	2.46 ± 0.19	12.98 ± 3.72	γ
		LN	$0.00021^{+0.00016}_{-0.00009}$	$0.062^{+0.013}_{-0.011}$	$0.0010^{+0.0001}_{-0.0001}$	$\mathbf{0.00011^{+0.00001}_{-0.00001}}$					
		LC	0.0	0.0	$0.61^{+0.04}_{-0.02}$	–					
58046.36 (11154)[a]	$1.36^{+0.01}_{-0.01}$	*LW*	$4.66^{+0.32}_{-0.32}$	$0.21^{+0.05}_{-0.04}$	$0.43^{+0.09}_{-0.06}$	–	166/234	–	–	7.91 ± 1.77	δ
		LN	$0.00086^{+0.00011}_{-0.00009}$	$0.013^{+0.004}_{-0.003}$	$0.0018^{+0.0003}_{-0.0002}$	–					
		LC	0.0	0.0	$3.26^{+0.02}_{-0.02}$	$6.32^{+0.07}_{-0.06}$					
58209.13 (13559)[a]	$1.43^{+0.01}_{-0.01}$	*LW*	$6.18^{+0.42}_{-0.35}$	$0.84^{+0.13}_{-0.11}$	$0.64^{+0.04}_{-0.04}$	$1.24^{+0.23}_{-0.21}$	171/232	–	–	24.02 ± 4.23	χ
		LN	$0.0059^{+0.0006}_{-0.0008}$	$0.018^{+0.002}_{-0.002}$	$0.016^{+0.001}_{-0.001}$	$0.00104^{+0.00012}_{-0.00011}$					
		LC	0.0	0.0	$2.20^{+0.01}_{-0.01}$	$4.42^{+0.03}_{-0.03}$					
58565.82 (18839)[a]	$1.52^{+0.01}_{-0.01}$	*LW*	$7.76^{+1.29}_{-0.81}$	$0.57^{+0.27}_{-0.15}$	$0.15^{+0.03}_{-0.01}$	$0.39^{+0.11}_{-0.09}$	130/232	–	–	21.14 ± 5.13	χ
		LN	$0.0045^{+0.0007}_{-0.0009}$	$0.014^{+0.003}_{-0.002}$	$0.031^{+0.004}_{-0.003}$	$0.0048^{+0.0009}_{-0.0008}$					

[a] Non-detection of HFQPO.

Table 3. Estimated rms% amplitudes of HFQPOs in different energy bands. All the errors are computed with a 68 per cent confidence level. See text for more details.

MJD (orbit)	HFQPO rms% amplitude (3−6 keV)	(6−25 keV)	(25−60 keV)	Non-detection of HFQPO (rms%) (3−60 keV)	Detection of HFQPO (HFQPO rms%) (3−60 keV)	Class
57451.89 (2351)[a]	–	–	–	0.54 ± 0.23	–	θ
57452.82 (2365)[a]	–	–	–	0.38 ± 0.11	–	χ
57453.35 (2373)[a]	–	–	–	0.44 ± 0.16	–	θ
57504.02 (3124)	0.39 ± 0.11	2.33 ± 0.25	0.81 ± 0.32	–	1.48 ± 0.36	ω
57552.56 (3841)[a]	–	–	–	0.61 ± 0.23	–	δ
57553.88 (3860)	0.79 ± 0.28	2.12 ± 0.22	0.88 ± 0.25	–	1.54 ± 0.48	δ
57689.10 (5862)[a]	–	–	–	0.16 ± 0.09	–	β
57705.22 (6102)[a]	–	–	–	0.86 ± 0.15	–	δ
57891.88 (8863)[a]	–	–	–	0.23 ± 0.12	–	ρ'
57892.74 (8876)[a]	–	–	–	0.77 ± 0.26	–	ρ
57943.69 (9629)[a]	–	–	–	0.94 ± 0.15	–	κ
57943.69 (9633)	0.38 ± 0.14	3.65 ± 0.31	0.56 ± 0.12	–	2.14 ± 0.50	κ
57946.10 (9666)	0.75 ± 0.18	3.34 ± 0.48	0.62 ± 0.21	–	2.55 ± 0.71	κ
57946.34 (9670)	0.83 ± 0.22	4.29 ± 0.54	0.71 ± 0.13	–	2.49 ± 0.37	κ
57961.39 (9891)[a]	–	–	–	0.82 ± 0.24	–	κ
57961.39 (9894)	0.79 ± 0.15	2.86 ± 0.29	0.77 ± 0.11	–	2.28 ± 0.63	κ
57961.59 (9895)	0.19 ± 0.07	3.12 ± 0.63	0.84 ± 0.33	–	1.98 ± 0.41	κ
57995.30 (10394)	0.72 ± 0.21	3.30 ± 0.55	0.67 ± 0.12	–	2.25 ± 0.31	ω
57996.46 (10411)	0.84 ± 0.24	4.01 ± 0.37	0.81 ± 0.15	–	2.66 ± 0.29	ω
58007.80 (10579)	0.68 ± 0.12	3.21 ± 0.42	0.89 ± 0.19	–	1.86 ± 0.37	ω
58008.08 (10583)	0.92 ± 0.16	3.64 ± 0.24	0.74 ± 0.21	–	2.46 ± 0.19	γ
58046.36 (11154)[a]	–	–	–	0.42 ± 0.14	–	δ
58209.13 (13559)[a]	–	–	–	0.76 ± 0.13	–	χ
58565.82 (18839)[a]	–	–	–	0.69 ± 0.11	–	χ

[a] Non-detection of HFQPO.

of the rms% amplitude to be 0.94 ± 0.15 (the rms% less than this value is considered to be 'insignificant QPO rms') for non-detection of HFQPO feature (see Table 3 and Fig. 4 for the PDS of the κ class). In contrast, we obtain the lowest value of rms% for the confirmed HFQPO detection as 1.48 ± 0.36 in the PDS. Accordingly, we identify 13 observations in the θ, β, δ, ρ, κ and χ variability classes that do not exhibit the signature of the HFQPO feature as presented in Table 3. Further, for reconfirmation (Belloni, Méndez & Sánchez-Fernández 2001; Sreehari et al. 2020), we include one additional Lorentzian in the PDS of orbit 9629 (κ class, as an example) by freezing the centroid frequency at 69.76 Hz and width at 5.01 Hz, similar to the HFQPO characteristics obtained in orbit 9666 (κ class), which has a similar exposure. The significance of the best-fitting Lorentzian feature is found to be 1.21 at 1σ unit, which indicates the non-detection of HFQPO. All the model-fitted parameters of the PDS are presented in Table 2. In Fig. 4, we show the model-fitted PDS corresponding to the θ, β, δ, ρ, κ and χ classes, modelled with Lorentzians and a constant. Note that in the wide frequency band, the PDS of the δ class observation (orbit 6102) shows a bump-like feature near 2 Hz, whereas the PDS corresponding to the κ class (orbit 9629) is completely featureless. We find a strong Type-C LFQPO at ∼5.05, ∼5.74 and ∼3.2 Hz for the θ, ρ and χ classes, respectively, whereas the LFQPO feature at ∼3.35 Hz is found to be broader for the β variability class. Here, we avoid a discussion of LFQPOs as it is beyond the scope of the present work.

3.3 Energy-dependent PDS

We study the energy-dependent PDS for all the 'softer' variability classes to examine the HFQPO features. While doing so, we divide the 3−60 keV energy band into different energy intervals and we search for HFQPO features following the same method as discussed in Section 3.2. We find that for the γ class observation, the HFQPOs are present only in 6−25 keV energy range with higher rms amplitude (∼3.64 per cent) and higher significance ($\sigma \sim 12$) at 1σ unit compared to that in the 3−60 keV energy band (see Tables 2 and 3). Futhermore, the PDS corresponding to the 3−6 and 25−60 keV energy bands are found to be featureless (see Fig. 5) as the rms% corresponding to the most significant peak is obtained as ∼0.92 and ∼0.74, respectively. In addition, we model the PDS in the 3−6 and 25−60 keV energy bands using the Lorentzian function with a centroid fixed at ∼72.32 Hz for the γ class (see Belloni et al. 2001; Sreehari et al. 2020). The highest values for the significance of the fitted Lorentzian are found to be 1.63σ and 0.7σ in the 3−6 and 25−60 keV energy bands, respectively. These results clearly indicate the non-detection of the HFQPO feature as the rms% values are insignificant. We follow same methodology for all the observations under consideration and find that the prominent HFQPO features are present only in the 6−25 keV energy range (see Fig. 5 and Table 3). In Fig. 5, the HFQPO feature is shown in each panel along with the non-detection cases in the insets. Moreover, we carry out a wide-band spectral analysis to understand the emission mechanisms that possibly manifest HFQPO signatures (see Section 4).

3.4 Dynamical PDS

The PDS in the different variability classes reveal that HFQPOs are not persistent but rather sporadic in nature. Therefore, we examine the dynamic nature of the PDS, where we search for the HFQPO in each segment of duration 32 s of the entire light curve of 1-ms

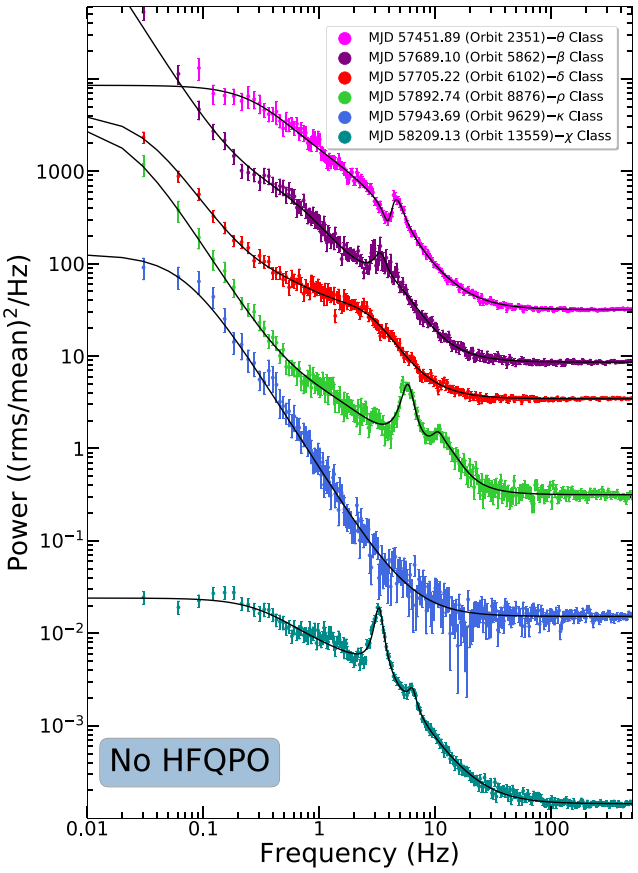

Figure 4. PDS of six different observations in the 3−60 keV energy band, where HFQPO is absent. Magenta, purple, red, green, blue and dark cyan circles denote the PDS corresponding to the θ, β, δ, ρ, κ and χ classes, respectively. For clarity, the PDS corresponding to the θ, β, δ, ρ and κ class observations are scaled by multiplying by 200 000, 50 000, 25 000, 2000 and 100. See text for details.

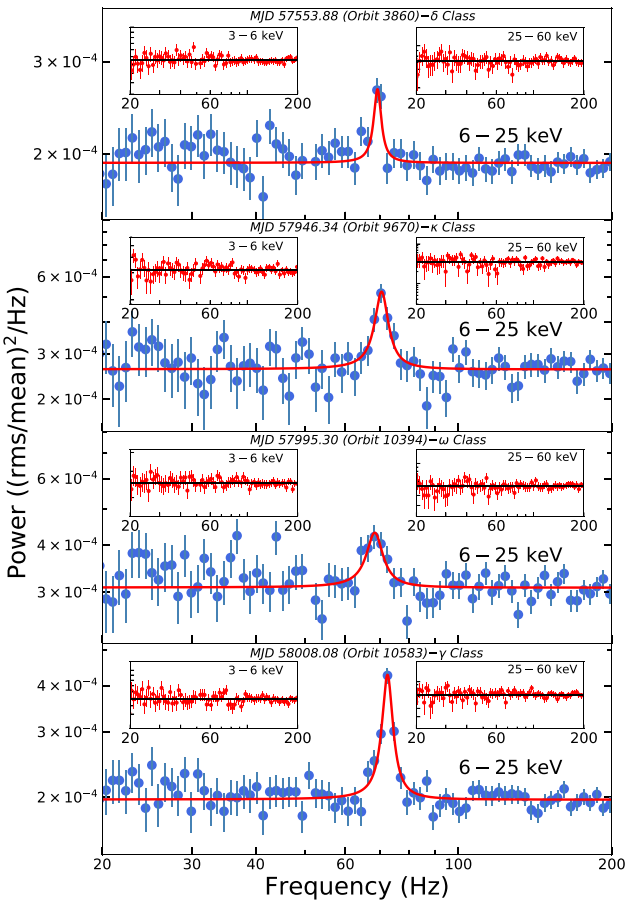

Figure 5. Energy-dependent PDS depicted in the 20−200 Hz frequency range. PDS corresponding to δ, κ, ω and γ class observations are presented in sequence from the top to bottom panels. Energy ranges are marked in each panel, including insets. The PDS corresponding to the 3−6 and 25−60 keV energy ranges are modelled with a constant, whereas the PDS in the 6−25 keV energy range is modelled using a constant and a Lorentzian. See text for details.

resolution. The Leahy power spectrum (Leahy et al. 1983) for each segment of the light curve is computed and plotted as a vertical slice corresponding to each time bin using the STINGRAY package[7] (Huppenkothen et al. 2019). The frequency bin size is chosen as 2 Hz. We use bicubic interpolation (Huppenkothen et al. 2019) to improve clarity and smoothen the dynamic PDS. The power corresponding to each frequency is colour coded such that yellow indicates minimum power and red indicates maximum power, as shown in the colour bar of Fig. 6.

In the left panels of Fig. 6, we present the light curve (top panel) of orbit 10411, generated by combining the LAXPC10 and LAXPC20 light curves along with the corresponding dynamic PDS (bottom panel). The light curve corresponds to the ω class variability (see Fig. 2). It is observed that the power at frequencies around 70 Hz is significant during 'non-dips' (high counts) and is insignificant during the 'dips' (low counts). The rms% amplitudes of the HFQPO during high counts and low counts are obtained as 2.38 ± 0.29 and 0.67 ± 0.18 for the ω class observation, respectively. This clearly suggests that the HFQPOs of frequencies around 70 Hz are generated when the count rate is high. We also observe similar behaviour during the γ class observation. From the right panels of Fig. 6, it is evident that the source emits at a high count rate of about 9000 cts s^{-1} throughout the observation. As a result, the HFQPO is seen to be present in almost every 32-s interval, although its power amplitude reduces during the narrow dips (500−700 s) present in the light curve. Overall, by analysing the dynamic PDS, we infer that within the 'softer' variability classes (κ, ω and γ), the high count rate (non-dips) seems to be associated with the generation of HFQPO features, as illustrated in Appendix A.

4 SPECTRAL ANALYSIS AND RESULTS

For each variability class, we generate the corresponding wide-band energy spectra combining the *SXT* and LAXPC20 data. We consider the 0.7−7 keV energy range for SXT spectra, whereas LAXPC spectra are extracted in the energy range of 3−50 keV (for details, see Sreehari et al. 2019, 2020). The dead-time corrections are applied to the LAXPC spectra while extracting with the LAXPCSOFT v3.4[8] software (Antia et al. 2017).

We model the wide-band energy spectra using XSPEC v12.10.1f in HEASOFT v6.26.1 to understand the radiative emission processes

[7] https://pypi.org/project/stingray/

[8] http://www.tifr.res.in/~astrosat_laxpc/LaxpcSoft.html

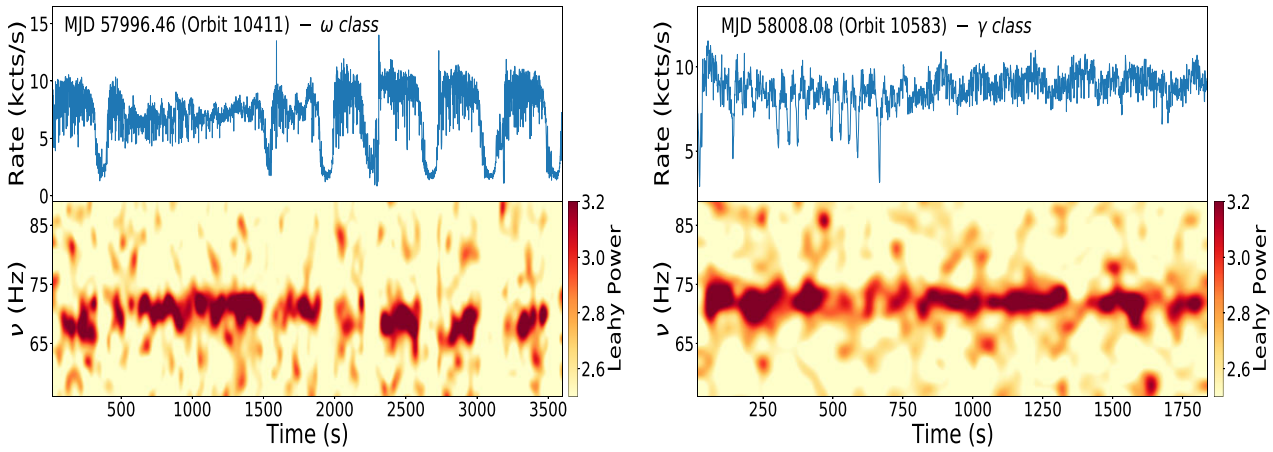

Figure 6. The light curves (3−60 keV) of the ω and γ classes are depicted in the top panels of each plot. The bottom panels of each plot present the dynamical PDS generated from the high-resolution (1-ms) light curve. Here, a 32-s segment size and 2-Hz frequency bin are used to represent the dynamical PDS. The obtained results are presented using the colour coding, where colour bars are given on the right of the bottom panels. See text for details.

active around the source. While modelling the energy spectra, we consider a systematic error of 2 per cent for both SXT and LAXPC data (Antia et al. 2017; Leahy & Chen 2019; Sreehari et al. 2020). We use the `gain fit` command in XSPEC to take care of the instrumental features at 1.8 and 2.2 keV in the SXT spectra. While applying `gain fit`, we allow the offset to vary and we fix the slope at 1. The hydrogen column density (*nH*) is kept fixed at 6×10^{22} atoms cm^{-2} following Yadav et al. (2016) and Sreehari et al. (2020).

To begin, we adopt a model `Tbabs×nthComp×constant` to fit the wide-band energy spectrum of the γ class observation (orbit 10583) for which the strongest HFQPO feature is seen in the PDS (bottom panel of Fig. 3). Here, the model `Tbabs` (Wilms, Allen & McCray 2000) takes care of the galactic absorption between the source and the observer. The model `nthComp` (Zdziarski, Johnson & Magdziarz 1996) represents the thermally Comptonized continuum. A constant parameter is used to account for the offset between the spectra from the two different instruments, SXT and LAXPC. The obtained fit yields a poor reduced χ^2 ($\chi^2_{\rm red} = \chi^2/{\rm dof}$) of 2095/546 = 3.83 as there are large residuals left at the higher energies beyond 30 keV. Hence, we include a power law along with one Xenon `edge` component at 32 keV (Sreehari et al. 2019) to fit the high-energy part of the spectrum. The Xenon `edge` is required for all the energy spectra to account for the instrumental absorption feature at 32−35 keV. Also, one `smedge` component is used at ∼9 keV to obtain the best fit. The model `Tbabs×(smedge×nthComp+powerlaw)×constant` provides a statistically acceptable fit with $\chi^2_{\rm red} = \chi^2/{\rm dof}$ of 563/533 = 1.08. In the left panels of Fig. 7, we present the best-fitting unfolded energy spectrum of the γ class observation for representation.

The best-fitting model parameters of the `nthComp` component for the γ class observation (orbit 10583) are obtained as electron temperature ($kT_{\rm e}$) $= 2.62^{+0.10}_{-0.12}$ keV and photon index ($\Gamma_{\rm nth}$) $= 2.02^{+0.06}_{-0.07}$ with normalization ($norm_{\rm nth}$) = 15 ± 2. The seed photon temperature ($kT_{\rm bb}$) is kept fixed at 0.1 keV during the fitting. The best-fitting value for the power-law photon index ($\Gamma_{\rm PL}$) is obtained as $\Gamma_{\rm PL} = 3.00^{+0.05}_{-0.06}$ with power-law normalization $norm_{\rm PL} = 21^{+4}_{-3}$. Following the same approach, we carry out the spectral modelling for all other observations of various variability classes (i.e. θ, β, δ, ρ, κ, ω, γ and χ) irrespective of the presence or absence of HFQPOs. The best-fitting model parameters are tabulated in Table 4. It is found that in all observations, the model `Tbabs×(smedge×nthComp+powerlaw)×constant` satisfactorily describes the energy spectra except for the ρ and χ class observations. For the ρ class, the acceptable fit is obtained without the power-law component, whereas in the χ class observation, an additional `diskbb` component is required along with `nthComp`. Note that we are unable to constrain the electron temperature for the observations of ρ, ρ' and two χ classes and hence we fix the electron temperature $kT_{\rm e}$ = 10 and 20 keV, respectively (see Table 4). In the right panels of Fig. 7, we present the wide-band energy spectra of two κ class observations on MJD 57961.39 (orbit 9891) and MJD 57961.59 (orbit 9895) without and with HFQPO feature, respectively. We point out that the best-fitting energy spectrum of orbit 9891 (without HFQPO) has a weak `nthComp` contribution ($norm_{\rm nth} \sim 7$), whereas in orbit 9895 (with HFQPO), the `nthComp` contribution ($norm_{\rm nth} \sim 16$) is relatively higher. We also find relatively high electron temperatures in these observations that confirm the detection of HFQPOs except for one observation in the θ class (orbit 2351).

Further, we estimate the flux in the energy range 0.7−50 keV associated with different model components used for the spectral fitting. While doing so, the convolution model `cflux` in XSPEC is used. For the γ class observation, the fluxes associated with the `nthComp` and `powerlaw` components are estimated as 2.49 and 1.37 in units of 10^{-8} erg cm^{-2} s^{-1}, respectively (see Table 4). We also calculate the bolometric flux ($F_{\rm bol}$) in the energy range 0.3−100 keV using the `cflux` model. Considering the mass ($M_{\rm BH}$) and the distance (d) of the source as $M_{\rm BH} = 12.4\,{\rm M}_\odot$ and $d = 8.6$ kpc (Reid et al. 2014), we calculate the bolometric luminosity in units of Eddington luminosity ($L_{\rm Edd}$)[9] as $L_{\rm bol} = F_{\rm bol} \times 4\pi d^2$. The luminosity is found to vary in the range of 3–34 per cent $L_{\rm Edd}$. The calculated flux values and bolometric luminosities for all the observations are given in Table 4.

In order to understand the nature of the Comptonizing medium in the vicinity of the source, we calculate the optical depth (τ) of the medium. Following Zdziarski et al. (1996) and Chatterjee, Agrawal & Nandi (2021), the relation among the optical depth (τ), `nthComp` spectral index ($\alpha = \Gamma_{\rm nth} - 1$) and electron temperature ($kT_{\rm e}$) is given

[9]Eddington luminosity $L_{\rm Edd} = 1.26 \times 10^{38} (M_{\rm BH}/{\rm M}_\odot)$ erg s^{-1} for a compact object of mass $M_{\rm BH}$ (Frank, King & Raine 2002).

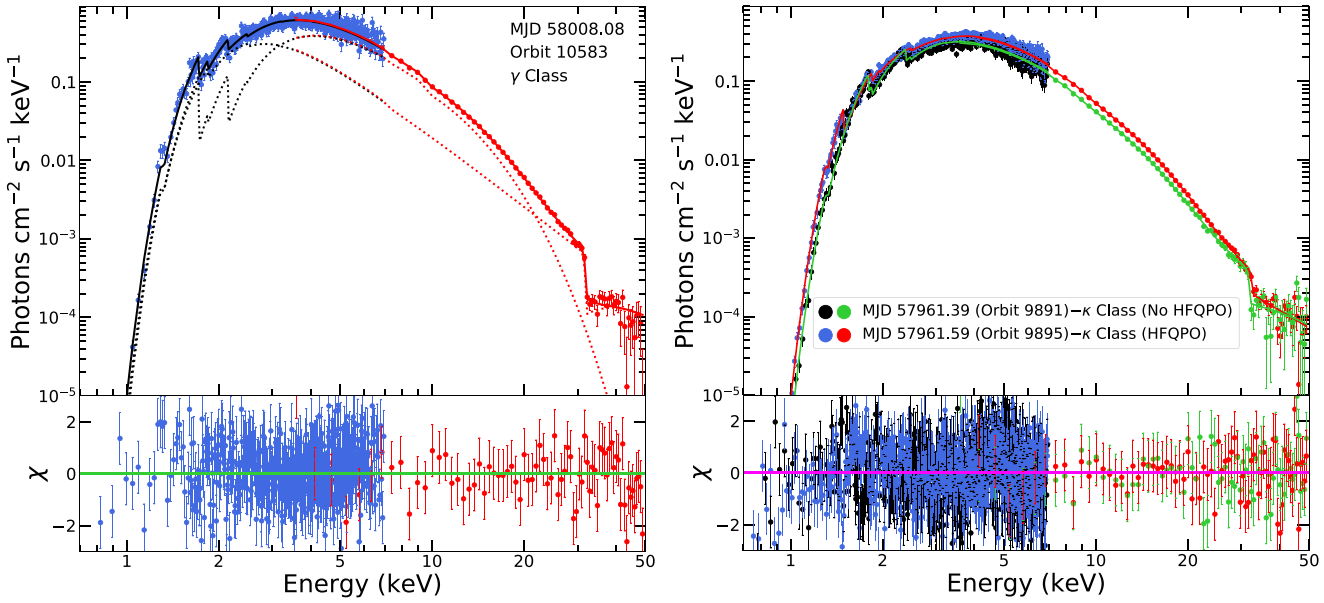

Figure 7. Unfolded wide-band (0.7−50 keV) energy spectra of the source GRS 1915+105. The spectra are modelled with `Tbabs×(smedge×nthComp+powerlaw)×constant`. The spectra of the γ class observation on MJD 58008.08 (orbit 10583) is presented in the left panels. Two best-fitting spectra of κ class variabilities without (MJD 57961.39; orbit 9891) and with (MJD 57961.59; orbit 9895) HFQPOs are depicted in the right panels. The bottom panel of each plot shows the residuals in units of σ. See text for details.

by

$$\alpha = \left[\frac{9}{4} + \frac{1}{(kT_{\rm e}/m_{\rm e}c^2)\tau[1+(\tau/3)]}\right]^{1/2} - \frac{3}{2}, \quad (1)$$

where $m_{\rm e}$ is the electron mass and c refers to the speed of light. Using equation (1), the optical depth (τ) is calculated and found in the range $2 \lesssim \tau \lesssim 14$ for all the observations. This implies that an optically thick corona is present as a Comptonizing medium in the vicinity of the source. Moreover, we calculate the Compton y-parameter, which measures the degree of Compton up-scattering of soft photons in the underlying accretion flow by the Comptonizing medium. Following Agrawal et al. (2018) and Chatterjee et al. (2021), the Compton y-parameter ($=4kT_{\rm e}\tau^2/m_{\rm e}c^2$) in the optically thick medium is found to be in the range between 0.63 ± 0.08 and 3.12 ± 0.35. In Table 4, we tabulate the obtained optical depth (τ) and Compton y-parameter values for all the observations.

5 SPECTRO-TEMPORAL CORRELATION

In this section, we examine the spectro-temporal correlation of the observed properties in different variability classes of GRS 1915+105. While doing so, we consider four variability classes (i.e. δ, κ, ω and γ), and study the variation of the rms% amplitude of HFQPO features as a function of energy, as shown in the top panel of Fig. 8. The results corresponding to the δ, κ, ω and γ classes are denoted by the filled triangles (blue), asterisks (yellow), squares (green) and circles (red), respectively. We find that HFQPO rms% increases with energy up to ∼17 keV and then sharply decreases. Further, to correlate the evolution of rms% with the Comptonized flux (i.e. `nthComp`), we present the variation of the estimated `nthComp` flux in the respective energy bands, as shown in the bottom panel of Fig. 8. We notice that `nthComp` flux decreases with energy and it becomes negligible beyond ∼25 keV (∼2 per cent of the total `nthComp` flux in 3−60 keV; see also Fig. 7).

In Fig. 9, we present the variation of photon index ($\Gamma_{\rm nth}$) with the `nthComp` flux ($F_{\rm nth}$) for observations in the δ, ρ, κ, ω, γ, β, and θ variability classes. Here, the variation of the rms% amplitude of the detected HFQPOs as well as the rms% of the non-detection of HFQPOs (see Table 3) are shown. We find that the rms% of HFQPOs lies in the range $\gtrsim$ 1.5 per cent and it drops below 1 per cent when HFQPOs are not seen. Further, we notice that in ω class observations, $\Gamma_{\rm nth}$ decreases with the increase of `nthComp` flux in the range $1.8 \times 10^{-8} \lesssim {\rm Flux_{nth}}$ (erg cm^{-2} s^{-1}) $\lesssim 4.5 \times 10^{-8}$. In κ variability classes, marginal variations are observed in the `nthComp` flux unlike the ω class observation, although photon indices remain at $\Gamma_{\rm nth} \gtrsim 2$ when HFQPOs are present. For δ variability classes, we find $3.5 \times 10^{-8} \lesssim {\rm Flux_{nth}}$ (erg cm^{-2} s^{-1}) $\lesssim 4.58 \times 10^{-8}$ and $\Gamma_{\rm nth} \gtrsim 1.9$ for HFQPOs. In addition, we point out that HFQPOs are not seen for the θ, β and ρ class observations although they belong to the 'softer' variability classes.

6 DISCUSSION

In this work, we carry out a comprehensive timing and spectral analyses of the BH-XRB source GRS 1915+105 using GT, AO and TOO data of the entire *AstroSat* observations (2016−2021) in wide frequency (0.01−500 Hz) and energy (0.7−60 keV) bands. The variation of the hardness ratios in the CCDs and the nature of the light curves confirm the presence of seven 'softer' variability classes (i.e. θ, β, δ, ρ, κ, ω and γ) along with one additional variant of ρ class (ρ') of the source (Athulya et al. 2022). The LAXPC count rates are found to vary in the range of 1328−10 997 cts s^{-1}, and the hardness ratios are seen to vary as $0.61 \lesssim$ HR1 $\lesssim 0.90$ and $0.02 \lesssim$ HR2 $\lesssim 0.11$. We also observe similar variabilities in the low-energy (0.7−7 keV) SXT light curves.

We examine the origin of the HFQPO features and find its presence only in four 'softer' variability classes (δ, ω, κ, γ). The centroid frequency and the rms% amplitude of the HFQPOs are found to vary in the range of 68.14−72.32 Hz and 1.48−2.66 per cent,

Table 4. Best-fitting parameters of the wide-band (0.7−50 keV) energy spectra of GRS 1915+105 with the model `Tbabs×(smedge×nthComp+powerlaw)×constant` for different observations, as mentioned in Table 1. In the table, kT_e is the electron temperature in keV, Γ_{nth} is the `nthComp` photon index and $norm_{nth}$ is the `nthComp` normalization. Γ_{PL} and $norm_{PL}$ are the power-law photon index and normalization, respectively. F_{nth} and F_{PL} are the flux in erg cm^{-2} s^{-1} associated with the `nthComp` and `powerlaw` components, respectively. F_{bol}, L_{bol}, τ and y-par are the bolometric flux, bolometric luminosity in units of $\%L_{Edd}$, optical depth and Compton y-parameter, respectively. All the errors are computed with a 90 per cent confidence level. See text for details.

MJD (orbit)	Model fitted parameters					χ^2_{red}	Estimated parameters						Class
	kT_e	Γ_{nth}	$norm_{nth}$	Γ_{PL}	$norm_{PL}$		F_{nth}	F_{PL}	F_{bol}	L_{bol}	τ	y-par	
	(keV)						(0.7−50 keV) (10^{-8} erg cm^{-2} s^{-1})		(0.3−100 keV)[a] (10^{-8} erg cm^{-2} s^{-1})	($\%L_{Edd}$)			
57451.89 (2351)[b]	$3.66^{+0.11}_{-0.12}$	$2.89^{+0.08}_{-0.05}$	34^{+3}_{-2}	$2.85^{+0.07}_{-0.07}$	42^{+4}_{-3}	1.14	2.51	2.84	5.38	30	6	0.83 ± 0.06	θ
57452.82 (2365)[b,c]	$23.92^{+7.54}_{-4.72}$	$2.57^{+0.03}_{-0.03}$	18^{+1}_{-1}	–	–	1.06	2.45	–	3.03	17	2	0.63 ± 0.08	χ
57453.35 (2373)[b]	$3.10^{+0.08}_{-0.07}$	$2.47^{+0.03}_{-0.02}$	29^{+4}_{-2}	$2.59^{+0.03}_{-0.03}$	23^{+2}_{-2}	1.08	2.85	3.14	6.05	34	7	1.29 ± 0.04	θ
57504.02 (3124)	$2.37^{+0.12}_{-0.11}$	$1.97^{+0.06}_{-0.05}$	16^{+3}_{-2}	$2.65^{+0.09}_{-0.08}$	4^{+2}_{-1}	1.18	4.46	0.44	5.06	28	12	2.47 ± 0.21	ω
57552.56 (3841)[b]	$1.94^{+0.04}_{-0.05}$	$1.83^{+0.06}_{-0.08}$	16^{+3}_{-4}	$3.27^{+0.05}_{-0.06}$	34^{+6}_{-7}	1.19	3.52	1.71	5.24	29	14	3.12 ± 0.35	δ
57553.88 (3860)	$2.53^{+0.10}_{-0.11}$	$2.08^{+0.09}_{-0.11}$	19^{+5}_{-5}	$3.18^{+0.05}_{-0.04}$	32^{+4}_{-3}	1.12	3.57	1.15	4.73	27	10	2.11 ± 0.31	δ
57689.10 (5862)[b]	$1.82^{+0.11}_{-0.09}$	$2.13^{+0.06}_{-0.06}$	12^{+4}_{-3}	$2.83^{+0.07}_{-0.07}$	20^{+4}_{-5}	1.11	1.64	1.91	3.85	22	12	2.06 ± 0.16	β
57705.22 (6102)[b]	$1.93^{+0.06}_{-0.04}$	$1.90^{+0.05}_{-0.05}$	15^{+4}_{-2}	$3.21^{+0.04}_{-0.03}$	24^{+3}_{-2}	1.08	2.37	1.67	4.26	24	14	2.80 ± 0.21	δ
57891.88 (8863)[b]	10[d]	$2.30^{+0.04}_{-0.02}$	9^{+2}_{-1}	–	–	1.22	1.03	–	1.05	6	–	–	ρ'
57892.74 (8876)[b]	10[d]	$2.86^{+0.04}_{-0.07}$	13^{+3}_{-2}	–	–	1.17	1.02	–	1.16	7	–	–	ρ
57943.69 (9629)[b]	$2.38^{+0.06}_{-0.06}$	$1.96^{+0.08}_{-0.07}$	6^{+1}_{-1}	$2.73^{+0.05}_{-0.05}$	2^{+1}_{-1}	1.02	1.04	0.59	1.65	9	12	2.51 ± 0.29	κ
57943.69 (9633)	$2.36^{+0.06}_{-0.05}$	$2.11^{+0.07}_{-0.09}$	7^{+1}_{-2}	$3.26^{+0.04}_{-0.03}$	15^{+3}_{-1}	1.18	1.06	0.52	1.57	9	11	2.04 ± 0.21	κ
57946.10 (9666)	$2.39^{+0.11}_{-0.08}$	$2.03^{+0.06}_{-0.05}$	7^{+2}_{-1}	$3.13^{+0.04}_{-0.04}$	13^{+3}_{-2}	1.03	1.21	0.54	1.76	10	11	2.27 ± 0.19	κ
57946.34 (9670)	$2.50^{+0.07}_{-0.06}$	$2.06^{+0.04}_{-0.04}$	7^{+1}_{-1}	$3.24^{+0.03}_{-0.03}$	16^{+1}_{-1}	1.17	1.10	0.55	1.78	10	11	2.17 ± 0.12	κ
57961.39 (9891)[b]	$2.48^{+0.09}_{-0.08}$	$1.97^{+0.06}_{-0.06}$	7^{+1}_{-1}	$2.80^{+0.05}_{-0.06}$	6^{+1}_{-2}	1.23	1.03	0.84	2.03	12	11	2.46 ± 0.21	κ
57961.39 (9894)	$2.64^{+0.10}_{-0.07}$	$2.10^{+0.07}_{-0.05}$	10^{+1}_{-1}	$3.05^{+0.05}_{-0.04}$	14^{+1}_{-1}	1.12	1.52	0.83	2.48	14	10	2.04 ± 0.19	κ
57961.59 (9895)	$2.77^{+0.11}_{-0.12}$	$2.23^{+0.07}_{-0.12}$	16^{+3}_{-2}	$3.12^{+0.05}_{-0.05}$	18^{+1}_{-1}	1.06	1.53	0.98	2.53	14	9	1.72 ± 0.25	κ
57995.30 (10394)	$3.06^{+0.13}_{-0.08}$	$2.44^{+0.05}_{-0.08}$	33^{+4}_{-5}	$3.12^{+0.04}_{-0.03}$	26^{+4}_{-2}	1.06	1.74	1.37	3.23	18	8	1.33 ± 0.12	ω
57996.46 (10411)	$3.07^{+0.11}_{-0.11}$	$2.36^{+0.05}_{-0.05}$	27^{+3}_{-3}	$3.13^{+0.04}_{-0.04}$	24^{+1}_{-1}	1.17	1.94	1.36	3.43	19	8	1.46 ± 0.08	ω
58007.80 (10579)	$2.67^{+0.09}_{-0.11}$	$2.17^{+0.06}_{-0.11}$	21^{+3}_{-4}	$3.10^{+0.03}_{-0.04}$	26^{+2}_{-1}	0.98	2.24	1.31	3.85	22	9	1.86 ± 0.14	ω
58008.08 (10583)	$2.62^{+0.10}_{-0.12}$	$2.02^{+0.06}_{-0.07}$	15^{+2}_{-2}	$3.00^{+0.05}_{-0.06}$	21^{+4}_{-3}	1.08	2.49	1.37	4.16	23	11	2.27 ± 0.22	γ
58046.36 (11154)[b]	$2.03^{+0.08}_{-0.06}$	$1.84^{+0.05}_{-0.05}$	15^{+3}_{-2}	$2.99^{+0.07}_{-0.06}$	14^{+2}_{-1}	1.25	3.36	1.68	5.12	29	14	3.05 ± 0.24	δ
58209.13 (13559)[b,c]	20[d]	$2.19^{+0.04}_{-0.04}$	8^{+1}_{-1}	–	–	0.93	2.21	–	2.34	13	–	–	χ
58565.82 (18839)[b,c]	20[d]	$1.88^{+0.02}_{-0.02}$	$0.71^{+0.03}_{-0.02}$	–	–	1.03	0.51	–	0.53	3	–	–	χ

[a] SXT response extends from 0.3 keV. [b] No detection of HFQPO. [c] Modelled with `diskbb` and `nthComp` components. Inner disc temperature, $T_{in} \sim 0.25$ keV.
[d] Frozen at 10 and 20 keV; below these values, the spectral fitting is affected, yielding higher χ^2_{red}.

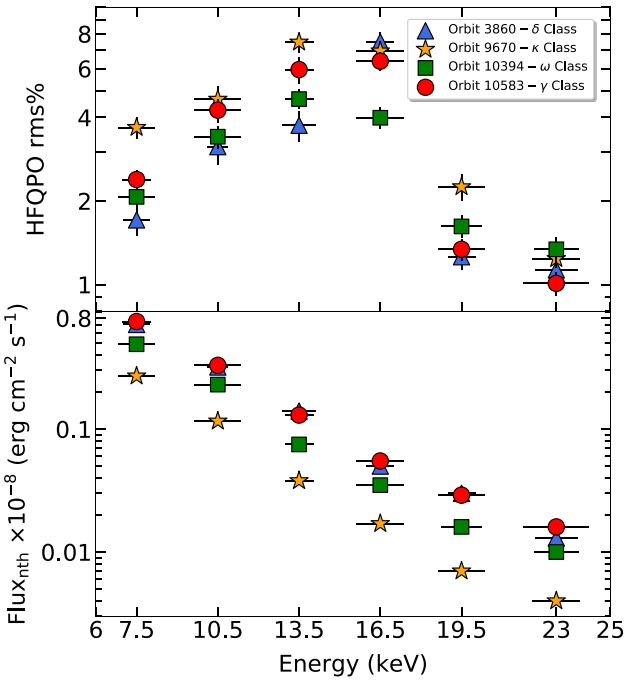

Figure 8. Top: variation of rms% amplitudes of HFQPOs with energy for the δ, κ, ω and γ variability classes. Bottom: variation of `nthComp` flux with energy corresponding to the variability classes as marked in the inset of the top panel. See text for details.

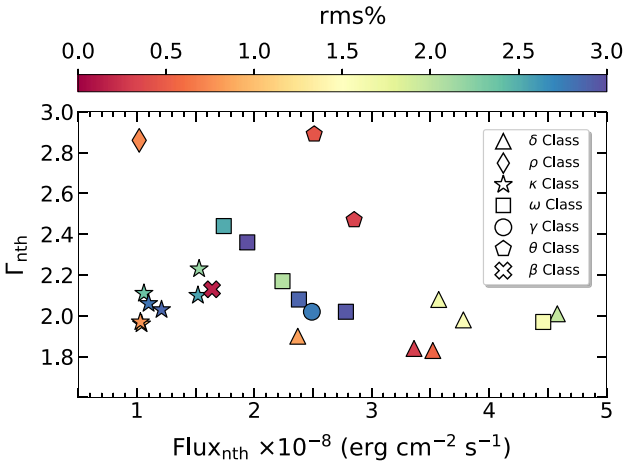

Figure 9. Variation of photon index ($\Gamma_{\rm nth}$) as a function of Comptonized flux associated with `nthComp` (see Table 4) for the $\delta, \rho, \kappa, \omega, \gamma, \theta$ and β variability classes. The colour coding denotes the rms% amplitudes corresponding to the detection and non-detection of HFQPOs. Obtained results for different variability classes are presented using different symbols, which are explained in the inset. See text for details.

respectively (see Tables 2 and 3). The present findings are consistent with the earlier results reported using *RXTE* observations (Belloni & Altamirano 2013a) as well as *AstroSat* observations (Belloni et al. 2019; Sreehari et al. 2020). It can be noted that the presence of additional peaks in the frequency range 27−41 Hz along with HFQPOs at 67−69 Hz was also observed (Belloni et al. 2001; Strohmayer 2001b) in GRS 1915+105. However, we do not find any signature of an additional peak in our analysis. Meanwhile, Morgan et al. (1997) and Strohmayer (2001b) noticed the evolution of frequency from ∼67 Hz to ∼69 Hz in the γ class, which is found to evolve further to $72.32^{+0.23}_{-0.21}$ Hz as seen in our observations (see Tables 2 and 3). This perhaps indicates the unique characteristics of the evolution of HFQPOs in a given variability class, which requires further investigation.

Next, we investigate the energy-dependent PDS to ascertain the photons that are responsible for the origin of the HFQPOs (see Fig. 5). We observe that HFQPO features are present in the 6−25 keV energy band in four variability classes (see Fig. 5 and Table 3). However, we do not find the HFQPO signature in the θ, β, ρ and χ variability classes (see Fig. 4 and Table 3). We find that the significance and rms% amplitudes of the HFQPOs are higher in the 6−25 keV energy band compared to the 3−60 keV energy band (see Table 3). Further, we study the variation of rms% amplitude and `nthComp` flux as a function of energy, as shown in Fig. 8. These findings are in agreement with the previous studies, which were carried out considering energy bands of 2−13 and 13−30 keV only (Belloni et al. 2001). It is also found that the `nthComp` flux gradually decreases with energy (see Fig. 8); beyond ∼25 keV, the flux contribution becomes negligible (see Fig. 7).

We notice that the κ and ω class variabilities exhibit different duration of 'non-dips' (high counts ∼9600 cts s^{-1}) and 'dips' (low counts ∼1250 cts s^{-1}) features. While studying the dynamic PDS, we find that the HFQPO is generally present during the period of 'non-dips' with relatively higher rms% amplitude (2.38 ± 0.29 and 2.35 ± 0.22 for the ω and κ classes). We do not find the signature of HFQPO during the 'dips' period, as seen in Fig. 6 (see also Appendix A). Similar findings are also observed for the γ class variability where the HFQPO is persistently seen during the entire high count duration (see also Belloni et al. 2001).

We find that the wide-band spectra (0.7−50 keV) of the θ, β, δ, κ, ω and γ class observations are satisfactorily described by the thermal Comptonization `nthComp` along with a power-law component (see Fig. 7 and Table 4). In contrast, the `nthComp` component seems to be adequate to fit the energy spectra of ρ class observations. From the spectral modelling, we obtain the range of the `nthComp` photon index as $1.83 \lesssim \Gamma_{\rm nth} \lesssim 2.89$, and the electron temperature as $1.82 \lesssim kT_{\rm e} \lesssim 3.66$ keV (see Table 4). In addition, we obtain a steep power-law photon index ($\Gamma_{\rm PL}$) as 2.59−3.27 for all the variability classes under consideration. A similar steep $\Gamma_{\rm PL}$ is also reported in the previous studies carried out for θ (Belloni et al. 2006) and δ (Sreehari et al. 2020) variability classes of the source. We estimate the optical depth (τ) of the surrounding medium and obtain its value as $2 \lesssim \tau \lesssim 14$. This evidently indicates the presence of a cool and optically thick corona around the source, which presumably acts as a Comptonizing medium that reprocesses the soft seed photons. The Compton y-parameter is obtained in the range between 0.63 ± 0.08 and 3.12 ± 0.35, which infers that the soft photons are substantially reprocessed via Comptonization at the optically thick corona. Further, we calculate the bolometric luminosity in the 0.3−100 keV energy range for all the variability classes and find its value in the range 3–34 per cent $L_{\rm Edd}$. These findings suggest that the source possibly emits in the sub-Eddington limit during the observations under consideration.

In Fig. 8, we examine the energy-dependent (6−25 keV) rms% of HFQPOs in the δ, κ, ω, and γ variability classes, and find that rms% increases (1–8 per cent) with energy up to ∼17 keV and then decreases. Subsequently, we observe that the Comptonization flux ($\rm Flux_{nth}$) decreases with energy, which tends to become negligible beyond 25 keV. This possibly occurs when the soft photons emitted from the disc are Comptonized by the 'hot' electrons from an

optically thick corona ($8 \lesssim \tau \lesssim 12$) and produce the aforementioned Comptonized continuum. In order to elucidate the spectra above ∼25 keV, an additional power-law component with photon index $\Gamma_{PL} \sim 3$ is required. This eventually indicates that there could be an extended corona present surrounding the central corona, which is responsible for this high-energy emission (Sreehari et al. 2020). We further notice that for the intermediate range of the `nthComp` photon index ($1.97 \lesssim \Gamma_{nth} \lesssim 2.44$) along with the large variation of `nthComp` flux, $1.06 \times 10^{-8} \lesssim \mathrm{Flux_{nth}}$ (erg cm^{-2} s^{-1}) $\lesssim 4.46 \times 10^{-8}$, generally yieldsthe HFQPO signature in the δ, κ, ω and γ variability classes (see Fig. 9). With this, we argue that the Comptonization process plays a viable role in exhibiting HFQPOs. Overall, based on the findings presented in Figs 8 and 9, we conjecture that HFQPOs in GRS 1915+105 are perhaps manifested due to the modulation of the 'Comptonizing corona' surrounding the central source (Méndez et al. 2013; Aktar et al. 2017, 2018; Dihingia et al. 2019; Sreehari et al. 2020).

Meanwhile, several theoretical models are put forward to explain the HFQPO features occasionally observed in BH-XRBs. Morgan et al. (1997) first attempted to elucidate the HFQPO features using the Keplerian frequency associated with the motion of hot gas at the innermost stable circular orbit (ISCO). This model yielded a high source mass of ∼30 $M_\odot$, which is not in agreement with the dynamical mass measurement of GRS 1915+105 (Greiner, Cuby & McCaughrean 2001; Reid et al. 2014) and hence is rejected (Belloni & Altamirano 2013a). Nowak et al. (1997) interpreted the origin of 67-Hz QPO in GRS 1915+105 as the resulting frequency of the lowest radial g-mode oscillation in the accretion disc. However, this model lacks cogency for those BH-XRBs that generally manifest >10 per cent rms amplitude variability. Further, there were alternative attempts to address the origin of HFQPOs without dwelling much on observational features (Chen & Taam 1995; Rezzolla et al. 2003; Stuchlík, Slaný & Török 2007). Noticing the significant hard lag in GRS 1915+105, Cui (1999) infer that a Comptonizing region is responsible for the HFQPOs. Remillard et al. (2002) further stressed the presence of a 'Compton corona' that reprocesses the disc photons and yields HFQPO features. In addition, Aktar et al. (2017, 2018) reported that the HFQPO features of GRO J1655−40 at 300 and 450 Hz perhaps resulted due to the modulations of the post-shock corona (PSC) that radiates Comptonized emissions (Chakrabarti & Titarchuk 1995). Recently, Dihingia et al. (2019) ascertained that shock-induced relativistic accretion solutions are potentially viable to explain the HFQPOs in well-studied BH-XRB sources, such as GRS 1915+105 and GRO J1655−40. With this, we can confirm that the HFQPO models proposed based on the 'Comptonizing corona' favour our observational findings delineated in this work.

7 CONCLUSIONS

In this paper, we perform in-depth temporal and spectral analyses in the wide-band (0.7−60 keV) energy range of the BH-XRB source GRS 1915+105 using the entire *AstroSat* observations (2016−2021) in seven 'softer' variability classes (i.e. θ, β, δ, ρ, κ, ω and γ) and one 'harder' variability class (χ), respectively. The overall findings of this work are summarized as follows.

(i) We find the HFQPO feature in the δ, κ, ω and γ classes of GRS 1915+105 that have a frequency in the range 68.14−72.32 Hz. However, we did not find the signature of HFQPO features in the θ, β, ρ, and χ class observations.

(ii) The study of energy-dependent PDS indicates that the emergent photons in the energy range 6−25 keV seem to be responsible for generating the HFQPO features. Beyond this energy range, the HFQPO signature is not detected. We notice that the rms% amplitude of HFQPOs increases (1–8 per cent) with energy up to ∼17 keV and then decreases.

(iii) The dynamical PDS of the κ and ω classes reveal that the 'non-dips' (high count) features of the light curve are possibly linked to the generation of HFQPOs.

(iv) The wide-band spectral modelling indicates that in the presence of HFQPOs, the thermal Comptonization components, $1.06 \times 10^{-8} \lesssim F_{nth}$ (erg cm^{-2} s^{-1}) $\lesssim 4.46 \times 10^{-8}$, which have $\Gamma_{nth} = 1.97-2.44$, dominate (up to ∼25 keV) over the additional power-law component, $0.52 \times 10^{-8} \lesssim F_{PL}$ (erg cm^{-2} s^{-1}) $\lesssim 1.37 \times 10^{-8}$, with $\Gamma_{PL} \sim 3$ (above ∼25 keV).

With the above findings, we argue that the variability produced during the 'softer' classes of GRS 1915+105 is possibly due to the modulation of the Comptonizing corona that manifests the HFQPO features.

ACKNOWLEDGEMENTS

The authors thank the anonymous reviewer for valuable comments and suggestions that helped to improve the clarity of the manuscript. SM, NA and SD thank the Department of Physics, IIT Guwahati, for providing the facilities to complete this work. NA, SD and AN acknowledge support from the Indian Space Research Organisation (ISRO) sponsored project, DS_2B-13013(2)/5/2020-Sec.2. AN thanks Group Head (Space Astronomy Group), Deputy Director (Payload, Data Management & Space Astronomy Area - PDMSA) and the Director (U R Rao Satellite Centre) for encouragement and continuous support to carry out this research. This publication uses data from the *AstroSat* mission of the ISRO, archived at the Indian Space Science Data Centre (ISSDC). This work has used data from the SXT developed at TIFR, Mumbai, and the SXT-POC at the TIFR is thanked for verifying and releasing the data and providing the necessary software tools. This work has also used data from the LAXPC Instruments developed at TIFR, Mumbai, and the LAXPC-POC at TIFR is thanked for verifying and releasing the data. We also thank the *AstroSat* Science Support Cell hosted by IUCAA and TIFR for providing the LAXPCSOFT software, which we used for LAXPC data analysis.

DATA AVAILABILITY

Data used for this publication are currently available at the Astrobrowse (*AstroSat* archive) website (https://astrobrowse.issdc.gov.in/astro_archive/archive) of the Indian Space Science Data Center (ISSDC).

REFERENCES

Abramowicz M. A., Kluźniak W., 2001, A&A, 374, L19
Agrawal P. C., 2006, Adv. Space Res., 38, 2989
Agrawal P. C. et al., 2017, J. Astrophys. Astron., 38, 30
Agrawal V. K., Nandi A., Girish V., Ramadevi M. C., 2018, MNRAS, 477, 5437
Aktar R., Das S., Nandi A., Sreehari H., 2017, MNRAS, 471, 4806
Aktar R., Das S., Nandi A., Sreehari H., 2018, J. Astrophys. Astron., 39, 17
Altamirano D., Belloni T., 2012, ApJ, 747, L4
Antia H. M. et al., 2017, ApJS, 231, 10
Antia H. M. et al., 2021, J. Astrophys. Astron., 42, 32
Athulya M. P., Radhika D., Agrawal V. K., Ravishankar B. T., Naik S., Mandal S., Nandi A., 2022, MNRAS, 510, 3019

Baby B. E., Agrawal V. K., Ramadevi M. C., Katoch T., Antia H. M., Mandal S., Nandi A., 2020, MNRAS, 497, 1197
Banerjee A., Bhattacharjee A., Chatterjee D., Debnath D., Chakrabarti S. K., Katoch T., Antia H. M., 2021, ApJ, 916, 68
Belloni T. M., Altamirano D., 2013a, MNRAS, 432, 10
Belloni T. M., Altamirano D., 2013b, MNRAS, 432, 19
Belloni T. M., Stella L., 2014, Space Sci. Rev., 183, 43
Belloni T., Klein-Wolt M., Méndez M., van der Klis M., van Paradijs J., 2000, A&A, 355, 271
Belloni T., Méndez M., Sánchez-Fernández C., 2001, A&A, 372, 551
Belloni T., Soleri P., Casella P., Méndez M., Migliari S., 2006, MNRAS, 369, 305
Belloni T. M., Sanna A., Méndez M., 2012, MNRAS, 426, 1701
Belloni T. M., Bhattacharya D., Caccese P., Bhalerao V., Vadawale S., Yadav J. S., 2019, MNRAS, 489, 1037
Beloborodov A. M., 1999, ApJ, 510, L123
Castro-Tirado A. J., Brandt S., Lund N., 1992, IAU Circ., 5590
Chakrabarti S., Titarchuk L. G., 1995, ApJ, 455, 623
Chatterjee R., Agrawal V. K., Nandi A., 2021, MNRAS, 505, 3785
Chen X., Taam R. E., 1995, ApJ, 441, 354
Cui W., 1999, ApJ, 524, L59
Cui W., 2000, ApJ, 534, L31
Dihingia I. K., Das S., Maity D., Nandi A., 2019, MNRAS, 488, 2412
Fender R. et al., 1999, ApJ, 519, L165
Frank J., King A., Raine D. J., 2002, Accretion Power in Astrophysics, 3rd edn. Cambridge Univ. Press, Cambridge
Greiner J., Cuby J. G., McCaughrean M. J., 2001, Nature, 414, 522
Haardt F., Done C., Matt G., Fabian A. C., 1993, ApJ, 411, L95
Hannikainen D. C. et al., 2005, A&A, 435, 995
Homan J., Wijnands R., van der Klis M., Belloni T., van Paradijs J., Klein-Wolt M., Fender R., Méndez M., 2001, ApJS, 132, 377
Homan J., Klein-Wolt M., Rossi S., Miller J. M., Wijnands R., Belloni T., van der Klis M., Lewin W. H. G., 2003, ApJ, 586, 1262
Homan J., Miller J. M., Wijnands R., van der Klis M., Belloni T., Steeghs D., Lewin W. H. G., 2005, ApJ, 623, 383
Huppenkothen D. et al., 2019, ApJ, 881, 39
Iyer N., Nandi A., Mandal S., 2015, ApJ, 807, 108
Katoch T., Baby B. E., Nandi A., Agrawal V. K., Antia H. M., Mukerjee K., 2021, MNRAS, 501, 6123
Klein-Wolt M., Fender R. P., Pooley G. G., Belloni T., Migliari S., Morgan E. H., van der Klis M., 2002, MNRAS, 331, 745
Klein-Wolt M., Homan J., van der Klis M., 2004, Nucl. Phys. B Proc. Suppl., 132, 381
Leahy D. A., Chen Y., 2019, ApJ, 871, 152
Leahy D. A., Darbro W., Elsner R. F., Weisskopf M. C., Sutherland P. G., Kahn S., Grindlay J. E., 1983, ApJ, 266, 160
Lucchini M. et al., 2021, preprint (arXiv:2108.12011)
Mandal S., Chakrabarti S. K., 2005, A&A, 434, 839
Markoff S., Nowak M. A., Wilms J., 2005, ApJ, 635, 1203
McClintock J. E., Remillard R. A., 2006, in Lewin W., van der Klis M., eds, Compact Stellar X-ray sources, Cambridge Astrophysics Series, No. 39. Cambridge Univ. Press, Cambridge, p. 157
Méndez M., Altamirano D., Belloni T., Sanna A., 2013, MNRAS, 435, 2132
Miller J. M. et al., 2001, ApJ, 563, 928
Mirabel I. F., Rodríguez L. F., 1994, Nature, 371, 46
Morgan E. H., Remillard R. A., Greiner J., 1997, ApJ, 482, 993
Nandi A., Manickam S. G., Rao A. R., Chakrabarti S. K., 2001, MNRAS, 324, 267
Nowak M. A., Wagoner R. V., Begelman M. C., Lehr D. E., 1997, ApJ, 477, L91
Nowak M. A. et al., 2011, ApJ, 728, 13
Poutanen J., Veledina A., Zdziarski A. A., 2018, A&A, 614, A79
Ratti E. M., Belloni T. M., Motta S. E., 2012, MNRAS, 423, 694
Reid M. J., McClintock J. E., Steiner J. F., Steeghs D., Remillard R. A., Dhawan V., Narayan R., 2014, ApJ, 796, 2
Remillard R. A., McClintock J. E., 2006, ARA&A, 44, 49
Remillard R. A., Morgan E. H., McClintock J. E., Bailyn C. D., Orosz J. A., 1999, ApJ, 522, 397
Remillard R. A., Muno M. P., McClintock J. E., Orosz J. A., 2002, ApJ, 580, 1030
Remillard R. A., McClintock J. E., Orosz J. A., Levine A. M., 2006, ApJ, 637, 1002
Rezzolla L., Yoshida S., Maccarone T. J., Zanotti O., 2003, MNRAS, 344, L37
Ribeiro E. M., Méndez M., de Avellar M. G. B., Zhang G., Karpouzas K., 2019, MNRAS, 489, 4980
Shakura N. I., Sunyaev R. A., 1973, A&A, 24, 337
Singh K. P. et al., 2017, J. Astrophys. Astron., 38, 29
Sreehari H., Ravishankar B. T., Iyer N., Agrawal V. K., Katoch T. B., Mandal S., Nand i A., 2019, MNRAS, 487, 928
Sreehari H., Nandi A., Das S., Agrawal V. K., Mandal S., Ramadevi M. C., Katoch T., 2020, MNRAS, 499, 5891
Strohmayer T. E., 2001a, ApJ, 552, L49
Strohmayer T. E., 2001b, ApJ, 554, L169
Stuchlík Z., Slaný P., Török G., 2007, A&A, 470, 401
Sunyaev R. A., Titarchuk L. G., 1980, A&A, 86, 121
Tanaka Y., Lewin W. H. G., 1995, in Lewin W. H. G., van Paradis J., van den Heuvel E. P. J., eds, X-ray Binaries. Cambridge Univ. Press, Cambridge, p. 126
Vadawale S. V., Rao A. R., Chakrabarti S. K., 2001, A&A, 372, 793
Vadawale S. V. et al., 2016, Proc. SPIE, 9905, 99051G
van der Klis M., 1988, in Ögelman H., van den Heuvel E. P. J., eds, NATO Advanced Science Institutes (ASI) Series C Vol. 262. Kluwer Academic, Dordrecht, p. 27
Wang J. et al., 2021, ApJ, 910, L3
Wilms J., Allen A., McCray R., 2000, ApJ, 542, 914
Yadav J. S. et al., 2016, Proc. SPIE, 9905, 99051D
Zdziarski A. A., Johnson W. N., Magdziarz P., 1996, MNRAS, 283, 193

APPENDIX A: INTENSITY-DEPENDENT POWER DENSITY SPECTRA

The power density spectra are generated separately considering both 'non-dips' (high counts) and 'dips' (low counts) durations of the light curve (orbit 10411, ω class). In the top panel of Fig. A1, we show the PDS corresponding to the 'non-dip' segment of the light curve, shown in the bottom-left inset in red. The HFQPO signature around $67.08^{+1.05}_{-1.35}$ Hz is distinctly visible (rms% $= 2.38 \pm 0.29$) in the top-right inset. In the lower panel, we plot the PDS obtained for the 'dip' segment of the light curve, which is indicated in red in the bottom-left inset. The HFQPO feature is not seen (rms% $= 0.67 \pm 0.18$), as shown in the top-right inset. We further confirm that similar findings are also observed during the κ class observation (orbit 9895), where the rms% of the HFQPO feature for 'non-dips' and 'dips' durations are obtained as 2.35 ± 0.22 and 0.26 ± 0.10, respectively.

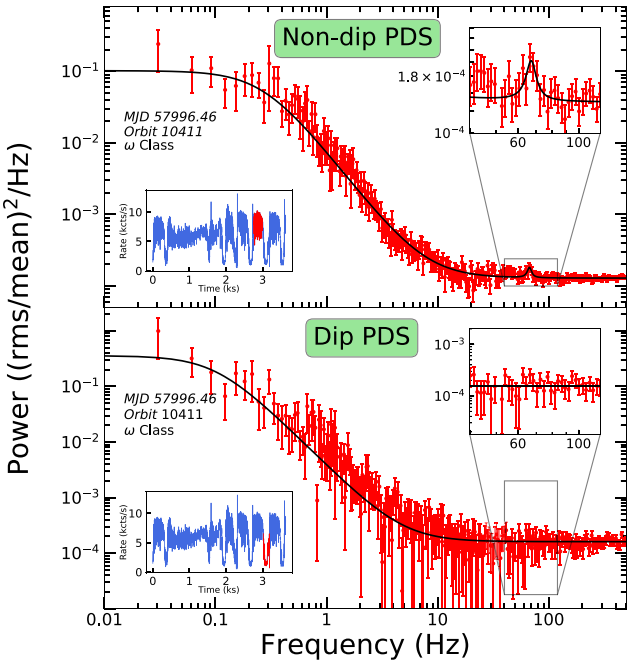

Figure A1. Top panel: PDS corresponding to one 'non-dips' (high counts) duration (red segment of the light curve) of the ω class observation (Orbit 10411) in a wide frequency range of 0.01−500 Hz. Bottom panel: PDS corresponding to one 'dips' (low counts) duration (red segment of the light curve). Both PDS are obtained for the energy band of 3−60 keV with LAXPC10 and LAXPC20 combined observations. In each panel, a zoomed view of the high-frequency region of the PDS is depicted in the inset.

This paper has been typeset from a TEX/LATEX file prepared by the author.